η-Carbides (Co, Mo, or W) Nanoparticles from Octacyanometalates Precursors-Based Network

Thomas Blin, Armelle Girard, Frédéric Fossard, Nathalie Guillou, Laure Catala, Annick Loiseau, Vincent Huc

η-carbides (Co, Mo or W) nanoparticles from octacyanometalates precursors-based network

Thomas Blin [1,2], Armelle Girard [1,3], Frédéric Fossard[1], Nathalie Guillou[4], Laure Catala[2], Annick Loiseau[1], Vincent Huc[2]*

1. Université Paris Saclay, UMR 104 ONERA-CNRS, LEM, F-92322, 92320 Châtillon, France
2. Institut de Chimie Moléculaire et des Matériaux d'Orsay (ICMMO), CNRS, Université Paris-Saclay, 91190 Orsay, France
3. Université de Versailles-Saint-Quentin-En-Yvelines (UVSQ), Université Paris-Saclay, 78000 Versailles, France.
4. Institut Lavoisier de Versailles (ILV), UMR CNRS 8180, UVSQ, Université Paris-Saclay, 78000 Versailles, France.

E-mail: thomas.blin@universite-paris-saclay.fr
armelle.girard@uvsq.fr
frederic.fossard@onera.fr
nathalie.guillou@uvsq.fr
laure.catala@universite-paris-saclay.fr
annick.loiseau@onera.fr
vincent.huc@universite-paris-saclay.fr

Keywords: Nanoparticles, carbides, octacyanometalates, bimetallic, η-carbides

Abstract

This paper describes a simple, two-steps chemical pathway to obtain bimetallic carbide nanoparticles (NPs) of general formula MxM'yC, also called η-carbides. This process allows for a control of the chemical composition of metals present in the carbides (M= Co and M'= Mo or W). The first step involves the synthesis of a precursor consisting of a network of octacyanometalates. The second step consists in a thermal degradation of the previously obtained octacyanometalates networks under neutral atmosphere (Ar or N2). It has been shown that this process results in the formation of carbide NPs with diameter of about 5nm, and the stoichiometries Co3M'3C, Co6M'6C, Co2M'4C for the Cs-Co-M' systems.

1. Introduction

Nanoparticles (NPs) have emerged as a key research topic in many fields of nanoscience. Among these fields we can mention hydrogen storage [1,2], agricultural production [3], some medical treatments [4], oil industry [5] and optics [6]. The field of chemical catalysis is one of those where the use of metal-based nanoparticles is widespread [7-9] due to their high reactivity related to their nanometric size, maximizing the surface/volume ratio. Within this framework, noble metal nanoparticles such as Au and Pt are well known and widely used for their catalytic properties. For instance, Au catalysts are used for hydrogenation reactions [10] or as support for semi-heterogeneous catalysts [11]. Because of the cost of these noble metals, different strategies are pursued to find surrogates to noble metals in catalysis [12]. One way is to employ bimetallic NPs such as Pt-Pd nanoalloys for the storage of hydrogen [13] or Pt-based core/shell NPs allowing dehydrogenation reactions [13]. Another emerging and promising approach is to play with NPs of transition metal carbides. Among the candidates for these substitutions are WC NPs [14,15], β-Mo_2C nanoparticles [16,17], MoWC anodes for proton exchange [18] or $Co_6Mo_6C_2$ combined with graphitic carbon for oxygen reduction [19]. Besides, the capability of metal carbides such as Fe_3C and bimetallic carbides such as Co_6W_6C to grow carbon nanotubes has also been reported and studied as a possible route to their selective synthesis in terms of chirality [20,21]. In short metal carbide nanoparticles are an important emerging topic in catalysis, both in terms of applications and understanding of their reactivity. In addition, the use of carbides has recently shown a growing interest in the synthesis of chemical compounds from biomass and thus using renewable resources, such as obtaining succinic acid using Mo_2C [22] or glycol obtaining from cellulose using W_2C [23].

However, progresses in this field are still slowed down by the difficulty to access to true, well characterized carbide nanoparticles.

Indeed, although several synthetic approaches exist to obtain the desired carbides, there are still obstacles to make them optimal. The syntheses are often done under harsh conditions. For example, the syntheses of NPs (size ranging from 30 to 70 nm) of TiC, V8C7, ZrC, Mo2C, WC compounds are done at 1000°C [24,25]. Moreover, the desired carbides are often observed to coexist with several other phases. R. André *et al*. [26] have described a synthetic method initiated at room temperature which produces transition metal carbides mixed with oxides and hydrides.

Our objective here is to present a new process for the synthesis of bimetallic carbide nanoparticles that is efficient, easy to implement and returns well defined nano-objects. We

focus our study on MxM'yC (M= Co and M'= Mo or W), also called η-carbides, chosen for their interest for several catalytic applications as introduced above. The usual synthesis route towards these bimetallic carbides uses mixed transition metals oxides as precursors. The main study concerning the synthesis of Co_3Mo_3C and Co_6Mo_6C is described by Newsam *et al* [27]. Molybdate salts are heated to 650 °C under He and H_2 flow and then heated to 1000 °C under CO/CO_2 to convert them into bimetallic carbides. Nevertheless, other synthetic routes reported in the literature were shown to form these compounds, including the one relying on Co_3Mo_3N nitride carburation [28,29].

The synthesis of carbide NPs presented in this work is a two-step process and the originality of this approach lies in the choice of the metallic precursors. Firstly, nanoparticles of cyanometallate precursor compounds (which belong to the family of Prussian Blue Analogs (PBAs [30,31])): octacyanometalates-based networks [32] (OCMs) are synthesized. The desired carbide nanoparticles are then obtained by thermal degradation of these OCM-type precursors, by adapting the carburation procedure developed by Aparicio et al. [33] for obtaining iron carbides from Prussian blue. This new synthetic route, and the associated characterization of the obtained carbide NPs are described throughout this article.

2. Octacyanometalates-based network (OCMs)

2.1. Synthesis

Octacyanometalate-based networks (OCMs) are three-dimensional metal networks in which the metals are linked together by C ≡ N bridges (**Figure 1**). A water-based surfactant-free synthesis was shown to be applicable for the synthesis of PBAs [34] and to a few OCMs nanoparticles [30] [35]. It is versatile enough to get networks composed of the combination of any transition metals of our choice. The main difference between PBAs and the less common OCMs lies in the choice of the reagent. In the case of PBAs, the reagents are hexacyanometallates, with metals bonded to 6 CN ligands, such as $K_3Fe(CN)_6$. The reagents used for OCMs are metals surrounded by 8 CN ligands, such as $K_4W(CN)_8$. The desired 3D compounds are obtained by mixing a solution of cyanometallates involving one kind of metal (M'= Mo or W) with a solution of another metallic salt of the second metal (M = Co) (Figure 1). The details of the synthesis are described in the experimental part. After the synthesis, the obtained nanoparticles are suspended in water. In order to recover the nanoparticles, an addition of a 2M solution of chloride calcium ($CaCl_2$) allows to retrieve the nanoparticles by centrifugation (10,000 rpm during 20 min), washed with

water and dried under vacuum. In the case of the Cs-Co-Mo system, the precipitate is brown, while for the Cs-Co-W system, appears red/brown.

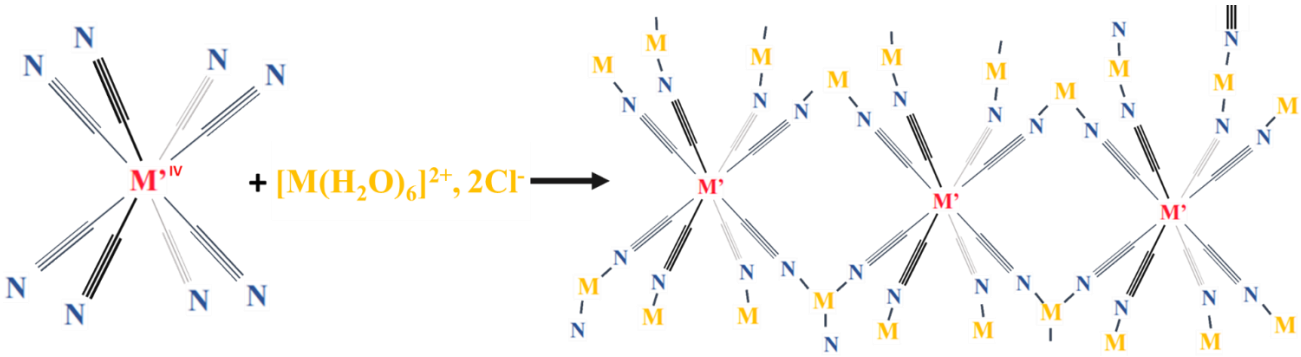

Figure 1. scheme of OCM synthesis from metals M (Co) and M' (Mo or W)

2.2. Structure

Power X-ray diffraction (XRD) was first used to identify the crystal structure and the lattice parameters of the synthesized OCM. **Figure** 2a shows the diffractograms of the Cs-Co-Mo and Cs-Co-W systems. Both patterns show the same diffraction peaks, which are, furthermore, identical to the one obtained by Hozumi et al. for $Cs_2Cu_7[Mo(CN)_8]_4,6H_2O$ [32]. The only differences lie in the relative intensity and width of the peaks due to the nature of the M' metal and the nanometric size of the grains. These similarities allow us to deduce that OCM present, whatever the M' metal, the same structural model, which is isostructural to $Cs_2Cu_7[Mo(CN)_8]_4,6H_2O$ [32] (see Figure 2b). Rietveld refinements of our two system have been undertaken by using TOPAS software [36] (figures S1 and 2). The unit cell parameters for each system (Cs-Co-Mo and Cs-Co-W) are very close to each other for both systems (see Table 1). The average crystallites size is estimated to about 9 nm and 8 nm for Cs-Co-W and Cs-Co-Mo, respectively. PXRD patterns of octacyanometalate networks without Cs referenced in the literature [37][38] do not match the experimental data of our compounds.

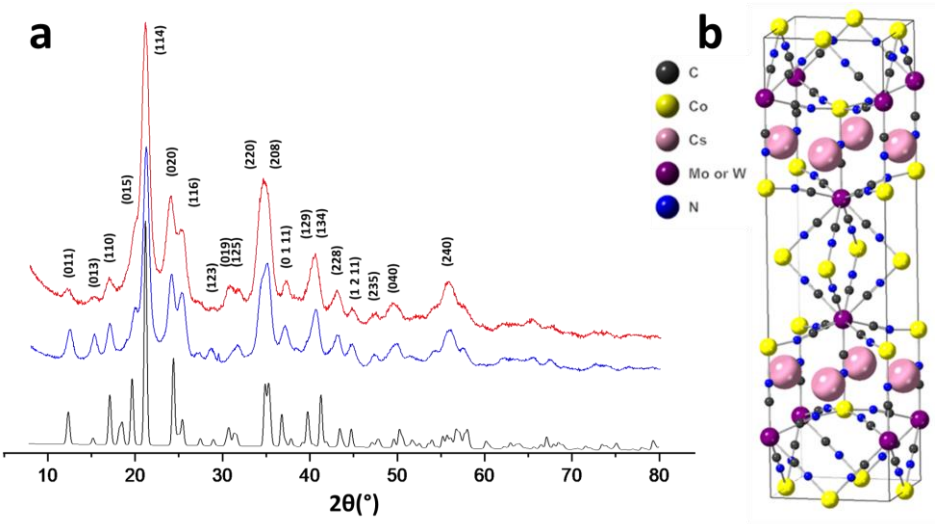

Figure 2. (a) PXRD data of the Cs-Co-W (blue) and Cs-Co-Mo (red) systems compared to the calculated data (black) from $Cs_2Cu_7[Mo(CN)_8]_4 \cdot 6H_2O$ structural model (b).

Transmission Electron Microscopy (TEM) reveals that OCM crystallites display two different morphologies, spherical and rod-like (**Figure 3**). The rods seem to bridge the spherical particles, suggesting that they have grown from them. Further, atomic imaging of their structure (inset of Figure 3b) recorded in Scanning Transmission Electron Microscopy in High Angle Annular Dark Field (STEM-HAADF) mode indicates that the growth occurred preferentially along the c direction. Characteristic distance ranging from 1.38 to 1.41 nm have been measured in different places of the networks (see an example in Figure 3b, insert)), which are very close to the expected inter-reticular distance d_{002} for the structure of $Cs_2Co_7[M'(CN)_8]_4 \cdot 6H_2O$, M'= Mo or W (TEM analysis performed on a Titan G2 microscope, see Experimental Methods).

The average size of the spherical NPs as well as the width of the rods is of the order of about 10 nm, attesting that their synthesis has been achieved at a nanoscale. It is in total agreement with what has been observed from PXRD. The dynamic light scattering (DLS) analysis of the nanoparticle dispersion in water shows (Figure S3) only one peak in the hydrodynamic size distribution by volume, which is centered around 11.68 nm for Cs-Co-Mo system and 14.55 nm for Cs-Co-W system.

Table 1. Crystallographic data of octacyanometalates-based network from the XRD data**.**

Precursor	Cs-Co-Mo	Cs-Co-W
Chemical formula	$Cs_2Co_7[Mo(CN)_8]_4 \cdot 6H_2O$	$Cs_2Co_7[W(CN)_8]_4 \cdot 6H_2O$
Formula weight (g/mol)	2002.75	2354.35
Crystal system	Tetragonal	Tetragonal
Space group	*I*4/*mmm*	*I*4/*mmm*
a (Å)	7.421(3)	7.417(3)
c (Å)	28.17(2)	28.29(2)
V, (Å^3)	1552(2)	1556(2)

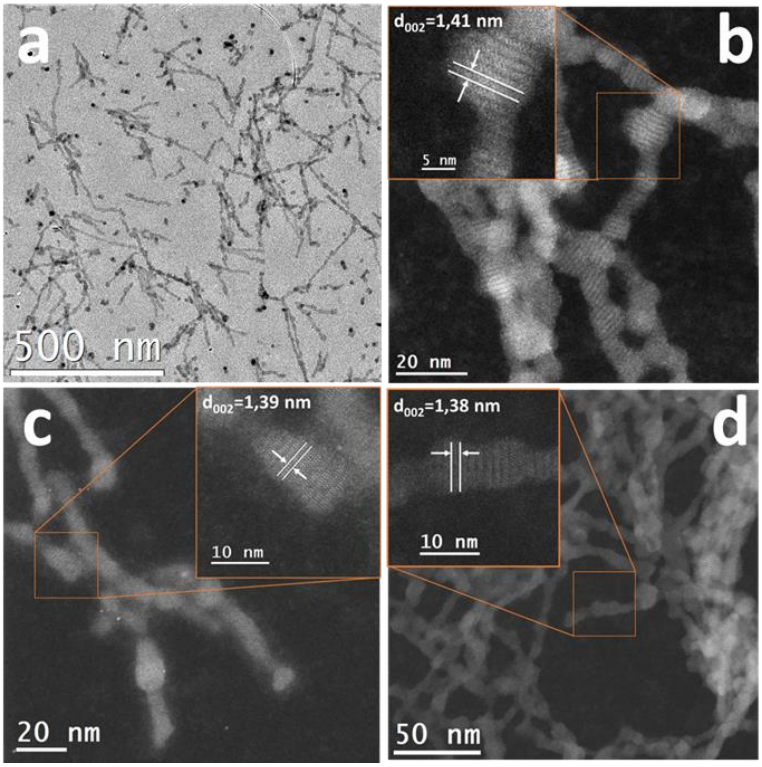

Figure 3. TEM imaging of Cs-Co-Mo octacyanometalates-based network (FEI - CM 20 TEM-200 kV). STEM-HAADF (Titan G2 microscope) imaging of octacyanometalates-based network of (a and b) Cs-Co-Mo highlighting in the inset a periodic spacing equal to 1.41±0.05 nm for the image (a) and 1.39±0.05 nm for image (b). (c) Cs-Co-W highlighting in the inset a periodic spacing equal to 1.38±0.07 nm

2.3. Chemical analysis

Energy Dispersive Spectroscopy (EDS) analysis of the Cs-Co-Mo and Cs-Co-W OCMs crystallites has been performed in a STEM. **Figure 4** shows elemental mappings related to Co and W for the Cs-Co-W OCM. The high concentration of metals (here Co and W) along the

rod-shaped nanoparticles is clearly seen. The expected ratio between Co and W (Co:W) based on the chemical formula $Cs_2Co_7[W(CN)_8]_4 \cdot 6H_2O$ is 7 atoms of Co for 4 atoms of W, i.e. 63.4 at. % of Co and 36.6 at. % of W. The experimental measurements on the ensemble of nanoparticles on the image (Table 2) obtained from the EDS analysis show that the observed proportions (W: 61.4±5.0% at and Co: 38.6±5.0% at) are close to these theoretical values. The elemental mappings related to Co and Mo for the Cs-Co-Mo OCM is given in the Figure S5 in the SI**.**

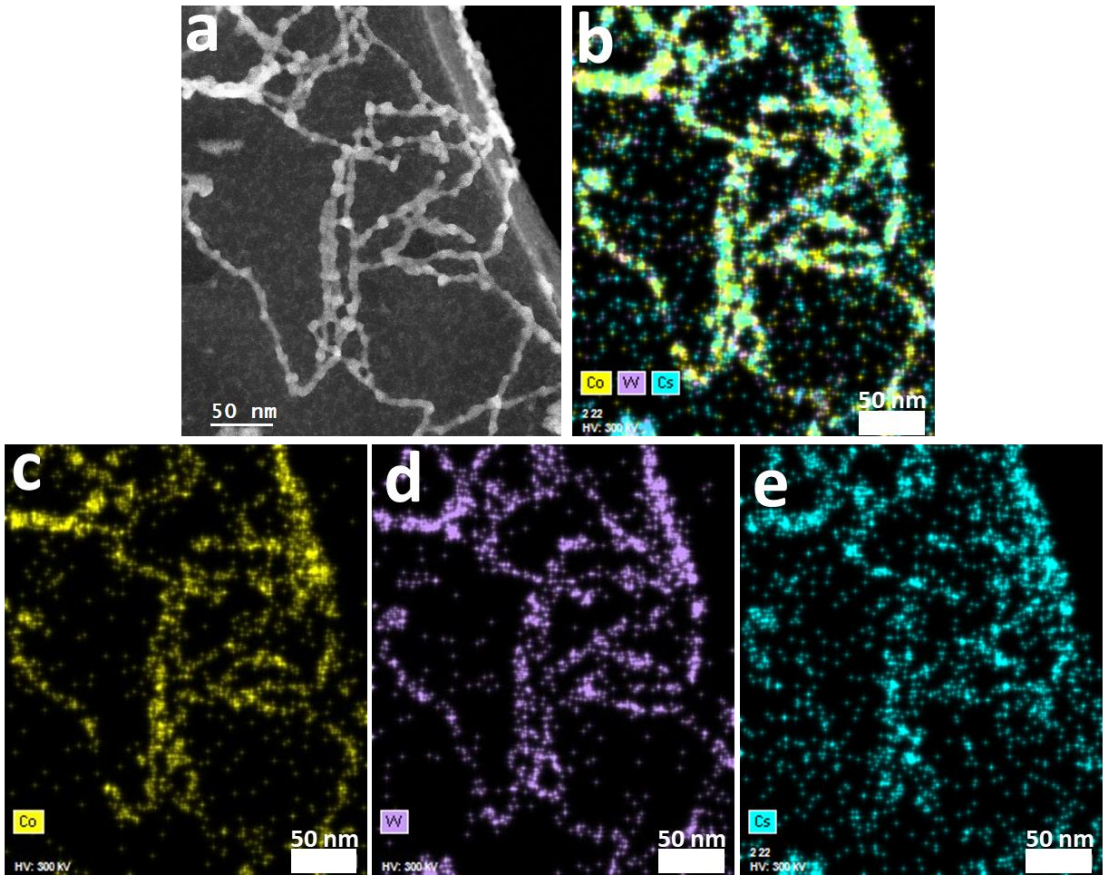

Figure 4. (a) Cs-Co-W OCM network HAADF-STEM image. (b), (c), (d) and (e) Corresponding EDS elemental mappings of Co-W-Cs, Co, W and Cs respectively (Co Kα1=6.930 KeV, W Lα1= 8.397 KeV, Cs Lα1= 4.286 keV)

Table 2. Comparison between the atomic percentages expected from the chemical formulas of the precursors and the atomic percentages deduced from EDS analyses**.**

Precursor	Cs-Co-Mo		Cs-Co-W	
Composition	Co(%)	Mo(%)	Co(%)	W(%)
Chemical formula	63.6	36.3	63.6	36.3
EDS analysis experimental	60 ± 5	40 ± 5	61 ± 5	38 ± 5

3. Synthesis and characterization of bimetallic η-carbides

3.1. Octacyanometalate network-based thermal treatment

The thermal decomposition of Prussian blue analogues is mainly influenced by the atmosphere composition during the thermal decomposition [39]. Using a reducing atmosphere, containing dihydrogen, would result in the formation of bimetallic nanoparticles [40] without crossing a carbide phase.

To turn the metalate network into metallic carbide, the procedure used by Aparicio *et al.* [33] was followed for obtaining iron carbides from Prussian blue. Cs-Co-Mo and Cs-Co-W OCMs were pyrolyzed under neutral atmosphere (N_2 or Ar). The mass losses consecutive to the thermal decomposition were followed by thermogravimetric analysis (TGA) as shown in **Figure** 5a, knowing that the initial molar mass of the precursor $Cs_2Co_7[Mo(CN)_8]_4{\cdot}6H_2O$ is 2002.77 g.mol^{-1} and 2354.33 g.mol^{-1} for $Cs_2Co_7[W(CN)_8]_4{\cdot}6H_2O$**.**

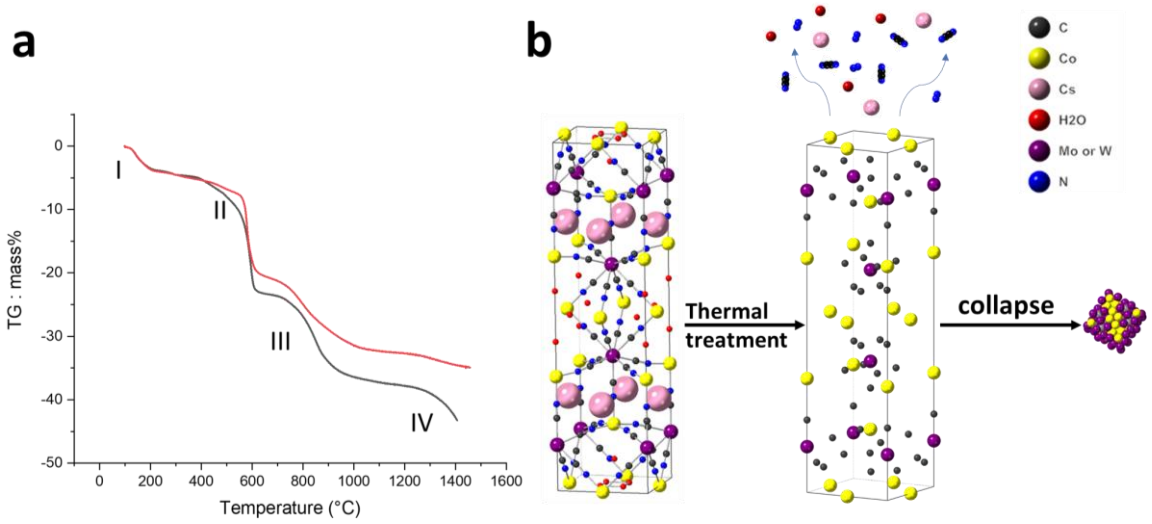

Figure 5. (a) Thermogravimetric analysis (TGA) of the octacyanometalates-based network: Cs-Co-Mo (black line) and Cs-Co-W (red line) systems. (b) Schematic view of the thermal degradation process of the octacyanometalates-based networks. Gas release and collapse occur simultaneously during thermal degradation**.**

The mass loss profile of OCMs is comparable to the one observed for Prussian blue [33]. Because of the great similarity between our curves and those presented by Aparicio *et al.* [33], it is likely that the nature of the eliminated gases is the same. On this comparative basis with Prussian blue

situation, step I is assigned to the loss of water molecules present in the sample, which represents about 5% theoretical mass for both compounds. Here, this loss is of the order of 3.3 %, still close to the expected value. Step II, between 200°C and 600°C is the first step of departure of cyanogen $(CN)_2$. It is characterized by a mass loss of 19.7% Cs-Co-Mo and 16.5% for Cs-Co-W OCMs. Step III, between 600°C and 900°C corresponds to the elimination of another part of cyanogen and nitrogen. During this step the compounds lose 32.3% of their mass for Cs-Co-Mo and 28.3% for Cs-Co-W. The departure of Cs during thermal degradation has been confirmed by EDS analysis of the nanoparticles, since Cs was not present on any samples after the thermal treatment (see Figure S7 in SI). At the end of step III, around 900°C, the total mass loss of the samples is 36.0% for Cs-Co-Mo and 32.4% for Cs-Co-W. According to Aparicio *et al.* [33], stage IV, starting in our systems above 900°C, corresponds to a departure of carbon not yet eliminated. Consequently, if pyrolysis is done below this temperature, a fraction of the carbon will remain in the system and is expected to lead to the formation of carbides**.**

The observation of samples after heating treatment of OCMs systems on TEM grids shows networks of aligned nanoparticles (**Figure 6**). These strings are expected to result from the in-place collapse of the previously observed rod-shaped OCMs precursors.

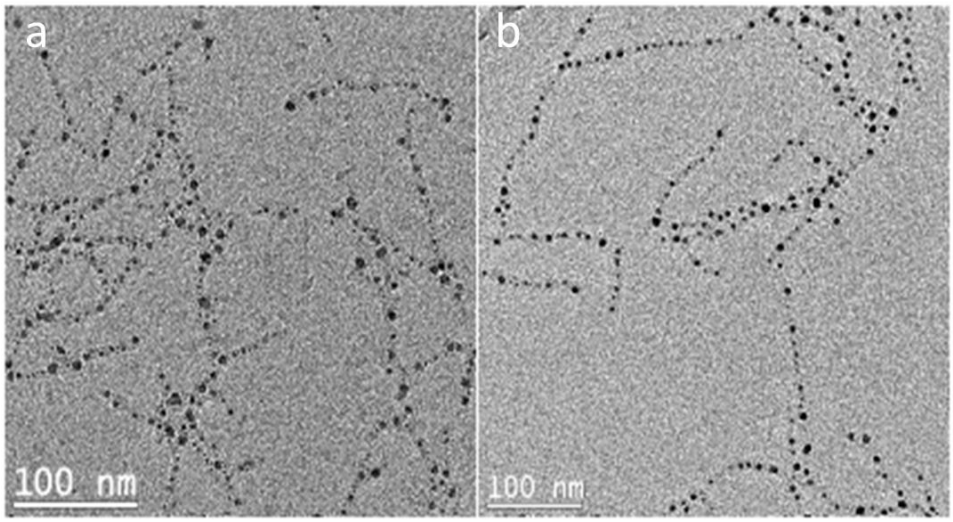

Figure 6. TEM images of nanoparticles strings obtained after pyrolysis at 800°C of the precursors (a) Cs-Co-Mo and (b) Cs-Co-W showing that the nanoparticles are located where the precursors were.

In order to confirm this in-place collapse mechanism, we performed in situ TEM observations of the thermal degradation of the OCMs by heating them gradually. Results presented in **Figure 7** for both systems, show that a minimum temperature is necessary to convert all the precursors into nanoparticles. For the Cs-Co-Mo system (Figure 7 a, b and c) the totality of the precursors

is not converted into nanoparticles at 500°C and it is necessary to reach at least 600-700°C to observe a full conversion of the OCMs into nanoparticles. In the case of Cs-Co-W (Figure 7 d, e, and f), traces of the precursors are still observed at 600°C and it is only around 800°C that the system is fully converted. In agreement with TGA analyses, these experiments confirm that it is necessary to reach a sufficiently high temperature (at least above 600°C) in order to ensure the departure of undesired elements (Cs and N), and to obtain a system without any trace of precursors. The collapse process is further clearly observed, resulting in the formation of NPs where the precursors were, hence their arrangement into strings**.**

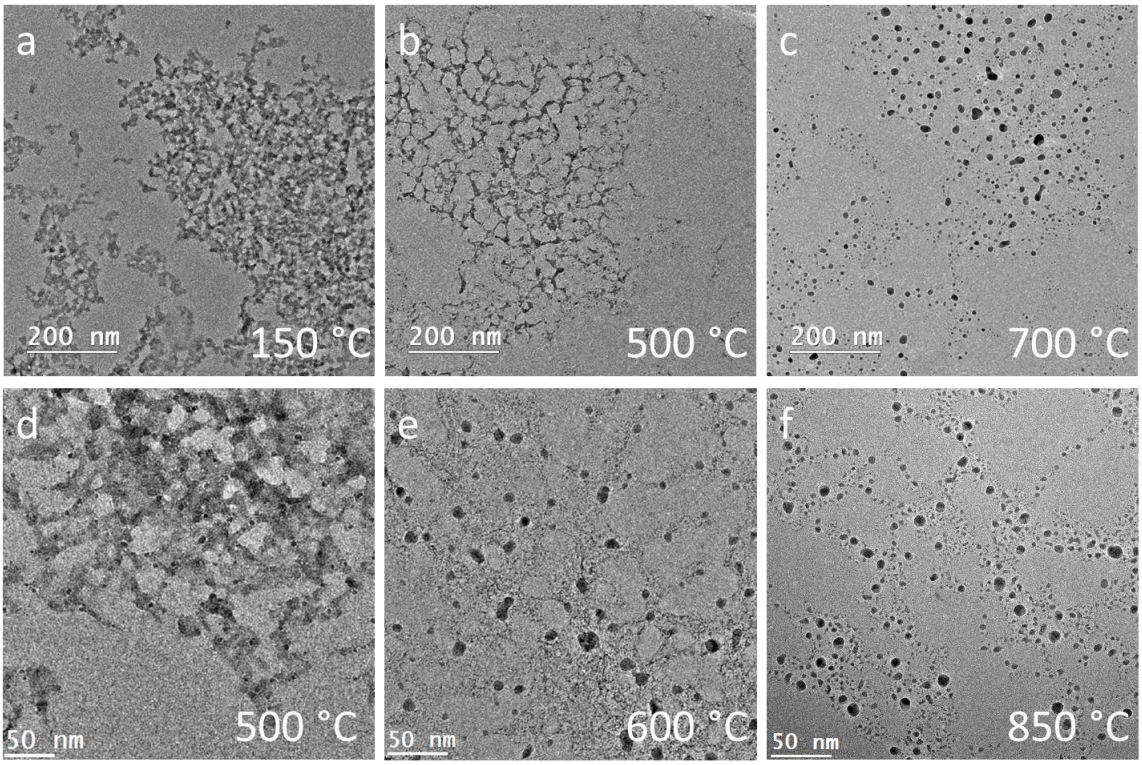

Figure 7. TEM imaging of the thermal decomposition of octacyanometalate networks. Pyrolysis *in-situ* monitoring of an area of the Cs-Co-Mo system at (a)150°C, (b) 500°C and (c) 700°C. Pyrolysis *in-situ* monitoring of an area of the Cs-Co-W system at (d) 500°C, (e) 600°C and (f) 850°C**.**

3.2. Characterization of nanoparticles obtained after pyrolysis of Cs-Co-Mo precursors.

Chemical composition of NPs resulting from the thermal treatment under neutral atmosphere are analyzed by EDS (**Figure 8**) and their structure from fast Fournier transform FFT analysis of HAADF STEM images. Four different groups of nanoparticles could be identified: monometallic Co, Janus-type nanoparticles (i.e., nanoparticles with two distinct phases), Mo_2C

carbides and Co-Mo bimetallic carbides called η-carbides. The proportion between these different phases depends on the pyrolysis temperature (Table 3). The η-carbides become predominant as soon as the pyrolysis temperature reaches 800°C. This is consistent with the previously discussed TG analysis (Figure 5a). The higher the temperature, the more carbide is present in the sample. An ideal pyrolysis temperature seems to be 900°C**.**

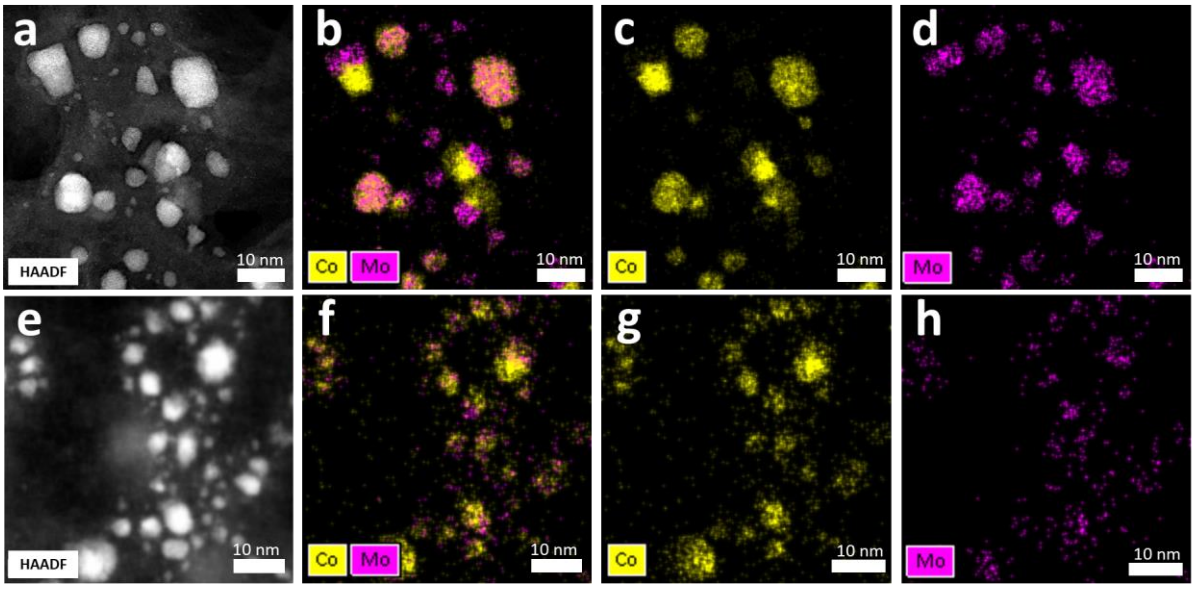

Figure 8. (a) HAADF-STEM image and (b, c and d) corresponding chemical mappings using EDS mode for Co-Mo system after pyrolysis under N_2 at 500°C. (e) HAADF-STEM image and (f, g and h) chemical mappings using EDS mode for Co-Mo system after pyrolysis under N_2 at 800°C.

Table 3. Population proportions and diameter evolution of Co, Janus, Mo_2C and η-carbide, nanoparticles as a function of pyrolysis temperatures of Cs-Co-Mo**.**

Pyrolysis temperature	NPs analyzed	NPs Co - proportion and average diameter (nm)		NPs Janus - proportion and average diameter (nm)		NPs Mo_2C - proportion and average diameter (nm)		η -carbide - proportion and average diameter (nm)	
500°C	84	6%	4.8±3.5	10%	5.7±1.9	57%	2.1±1.4	27%	4.7±1.8
600°C	198	0	/	3%	5.1±0.7	42%	1.9±0.7	55 %	3.4±1.1
800°C	377	0	/	9%	5.8±1.6	29 %	2.0±0.8	62%	2.6±1.1

An extensive statistical analysis of the particle size according to their phase nature, is summarized in Table 3. The diameter of Mo_2C nanoparticles varies in average between 1.8 and 2.15 nm. The Janus nanoparticle maintains a diameter between 5 and 6 nm. On the other hand,

the η-carbide nanoparticles have a diameter that decreases sharply when increasing the pyrolysis temperature (Table 3).

The Janus nanoparticles consist of a Co phase and another phase which is either a bimetallic carbide or Mo_2C. **Figure 9** shows the analysis of a typical Janus nanoparticle. The phase at the bottom is identified as pure Co (in yellow), while the upper part of the NP is composed of 30±5 at. % Co and 70±5 at. % Mo. The HAADF image reveals for the upper phase a complex fringe structure. According to its FFT analysis (Figure 9b), the fringe periodicity can be assigned to (111) planes of the Co_2Mo_4C structure while fringes of the lower part of the NP are corresponding to (101) planes of Co. The Janus type nanoparticles do not exceed 10% of the population, whatever the annealing temperature, and are thus minority.

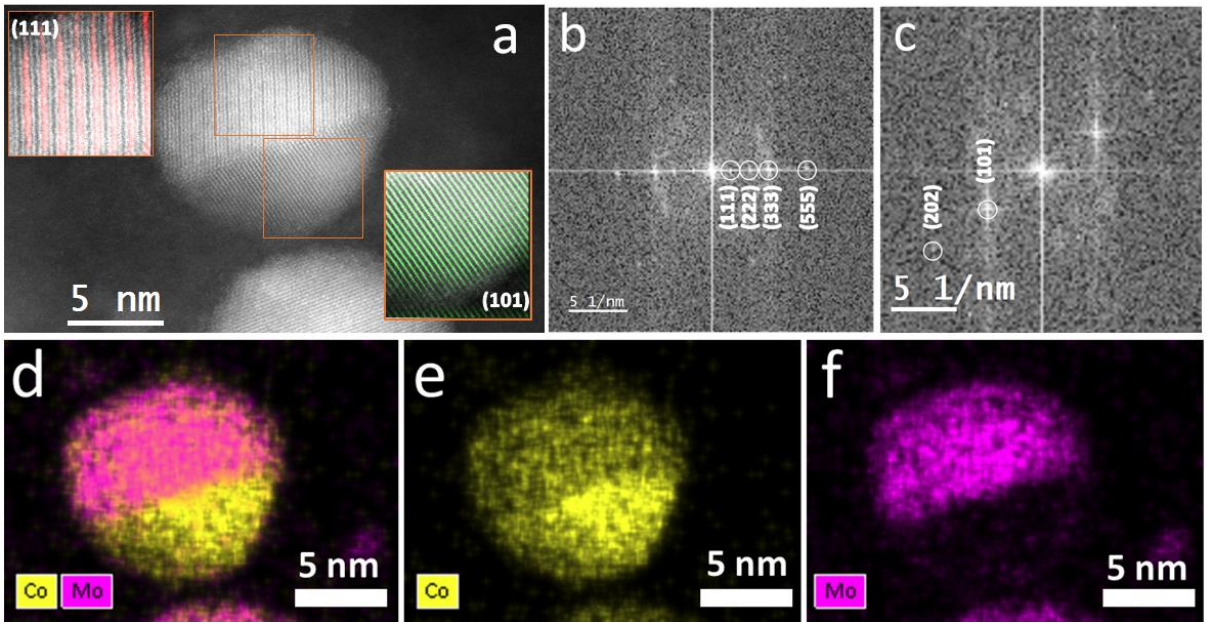

Figure 9. (a) HAADF-UHRSTEM image of a Janus nanoparticle marked by the orange square observed after pyrolysis of the Cs-Co-Mo precursor. The upper phase consists of the Co_2Mo_4C structure, with the (111) plane highlighted. the lower phase consists of the Co structure, with the (101) plane highlighted. (b) FFT of the upper phase showing diffraction peaks consistent with the Co_2Mo_4C structure. (c) FFT of the lower phase consistent with the Co structure. (d, e, and f): EDS elemental mappings highlighting the spatial distribution of Co and Mo within the nanoparticle.

In bimetallic particles, different types of η-carbides-type structures were evidenced: Co_3Mo_3C, Co_6Mo_6C and Co_2Mo_4C (see their crystallographic data in Table S1 of the SI). An example of analysis of a NP with the Co_6Mo_6C crystal structure is presented in **Figure 10**. Elemental EDS mappings (Figure 10 b and c) show a homogeneous distribution of Co and Mo in the proportion

Co: 54±5 at. % and Mo: 46±5% within the NP. Furthermore, the HAADF-STEM image (Figure 10a) is identified as the projection of the Co_6Mo_6C structure along its [110] zone axis (Figure 10d). A simulation of the HAADF image was performed using the Co_6Mo_6C crystal structure model in the [110] zone axis using the experimental illumination conditions (Figure 10e). The simulated image is very similar to the magnified experimental one (Figure 10f). In particular, atoms with the highest contrast are Mo atoms which form a pattern closely matching the most intense dots of the experimentally observed one, attesting the reliability of the structure assignment. This assignment is also confirmed by comparing the FFT of the HAADF-STEM image and the simulated electron diffraction of the of Co_6Mo_6C in the [110] zone axis (see Figure S81 in SI).

Differentiation between Co_3Mo_3C and Co_6Mo_6C carbides is not always possible, because both crystal structures have the same Co:Mo stoichiometry which cannot be discriminated by EDX. Moreover, the orientation of the nanoparticles does not always enable the identification of relevant atomic planes. Co_2Mo_4C can be distinguished from other structures because of its characteristic Co/Mo ratio. **Table 4** compares the percentage of Co_2Mo_4C with other bimetallic carbides in the samples as a function of pyrolysis temperature. An increase in the proportion of Co_2Mo_4C (example of identification in the Figure S9 in SI) with increasing pyrolysis temperature is observed. Co_3Mo_3C/Co_6Mo_6C represents the most important part of the bimetallic carbides present in the samples.

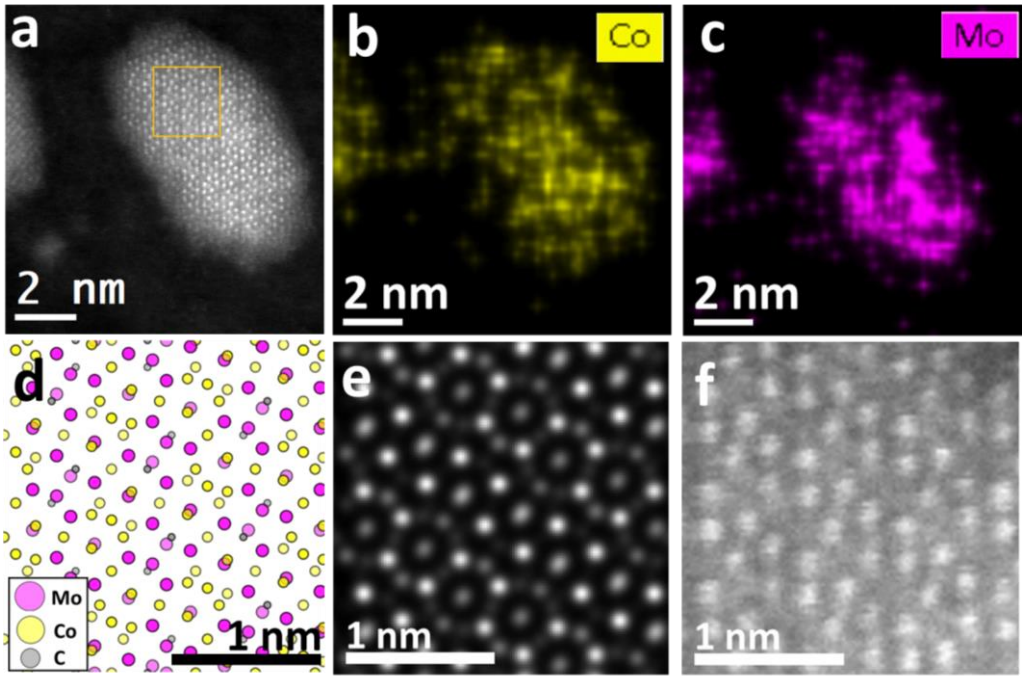

Figure 10. Analysis of a NP with the Co_6Mo_6C structure (a) HAADF-STEM image of the nanoparticle. (b and c) Elemental Co and Mo EDS mappings. (d) Co_6Mo_6C structure projected along the [110] zone axis. (e) Simulated HAADF-STEM image with Dr.Probe software[41]. (f) zoom over the experimental image (zoomed area indicated as a rectangle in (a))**.**

Table 4. Proportion of observed η-carbides from the Co-Mo system as a function of temperature.

Pyrolysis temperature	Co_2Mo_4C	Co_3Mo_3C / Co_6Mo_6C
500°C	9%	91%
600°C	28%	72%
800°C	34%	66%

3.3. Characterization of nanoparticles obtained after pyrolysis of Cs-Co-W precursors.

For the Cs-Co-W system, three different groups of nanoparticles: Janus NPs, WC and the targeted η-carbides (**Figure 11**) have been identified. Crystallographic data of the different possible η-carbides are given in Table S2 in SI. Note that monometallic (i.e., isolated) pure Co particles were not present among the NPs analysed.

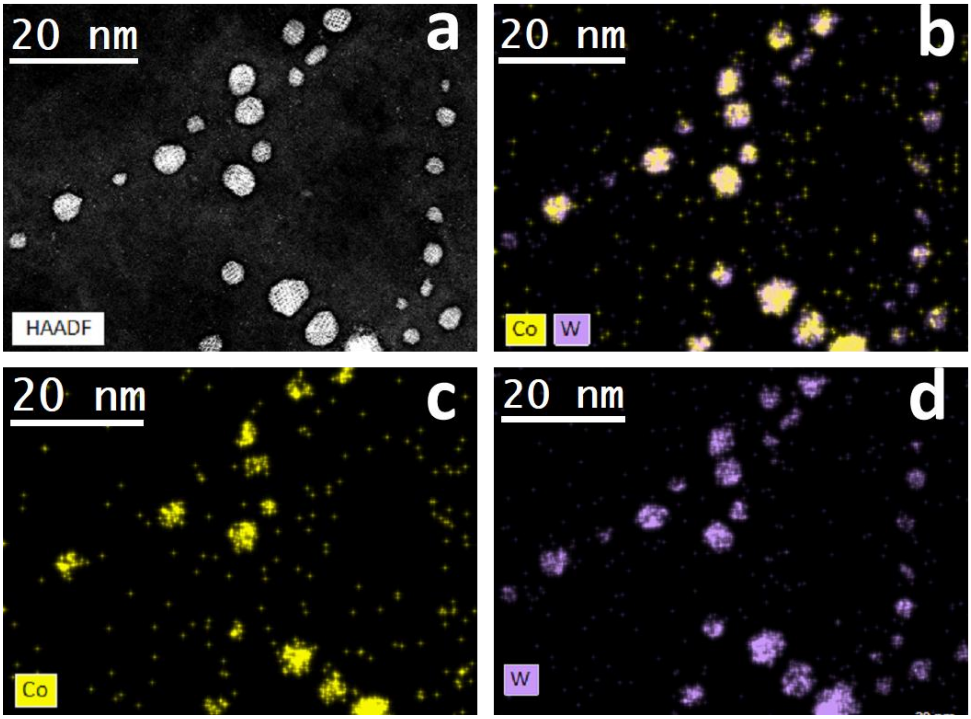

Figure 11. (a) HAADF image of NPS after pyrolysis under N_2 at 800°C of the Cs-Co-W system and (b, c, d) corresponding EDS elemental mappings (W is purple Co is yellow).

Table 5 summarizes the relative amount of these three kinds of NPs as a function of the pyrolysis temperature. As for the Cs-Co-Mo system, the higher the temperature, the higher the amount of NPs with a carbide phase. Interestingly, a very significant proportion of η-carbide phases is already present in the sample annealed at 500°C although the precursors are not yet fully degraded according to our *in-situ* TEM experiments (Figure 8).
Moreover, for this system, the average diameter of the observed nanoparticles varies greatly with the annealing temperatures in a random manner (**Table 5**).

Table 5. Proportions and diameter evolution of Janus, WC and η-carbide, nanoparticles as a function of pyrolysis temperatures for the Cs-Co-W system.

Pyrolysis temperature	NPs analyzed	NPs Janus– proportion and average diameter (nm)		Carbide WC– proportion and average diameter (nm)		η -carbide – proportion and average diameter (nm)	
500°C	177	3%	4.3±0.8	7%	2.0±0.8	90%	3.1±1.1
600°C	347	8%	8.3±2.4	54%	1.4±1.3	38%	6.9±2.4
800°C	268	0%	/	30%	4.5±1.4	70%	2.7±1.4

Janus-type nanoparticles are composed of two phases, one being a bimetallic carbide and the second one either pure Co or another bimetallic carbide. This latter situation is illustrated in **Figure 12**: one phase is a η-carbide phase, possibly Co_3W_3C or Co_6W_6C, the second one is a W-rich η-carbide phase, possibly Co_2W_4C. WC carbide was never observed in the Janus-type NPs, in contrast with the Co-Mo system, for which Janus NPs could involve the Mo_2C phase.

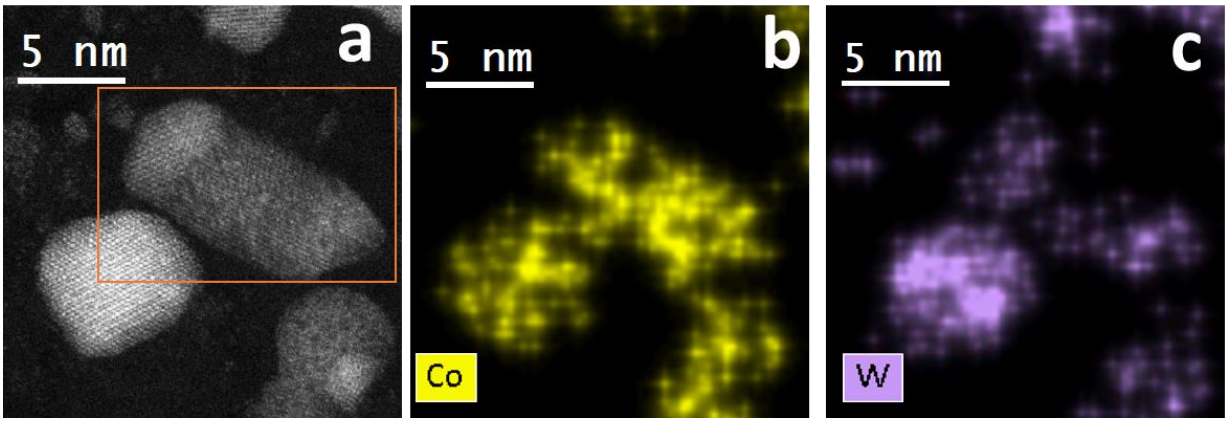

Figure 12. (a) HAADF-UHRSTEM image of a Janus nanoparticle marked by the **orange** square of Janus type nanoparticles synthesis with Co-W-C system. (b) (c) EDS analysis with elemental mappings of W in purple and the one of Co in yellow. The NP consists possibly of a Co_6W_6C or Co_3W_3C with 55±5% of Co and 45±5% of W (left part of (a)) and the phase (right

part of (a)) identified as Co_4W_2C with 71±5% of Co and 29±5% of W. The HAADF identification is in the Figure S11 in SI

Regarding NPs with a η-carbide phase, four structures are observed: Co_3W_3C, Co_6W_6C, Co_4W_2C and Co_2W_4C. **Table 6** shows the proportions of these different carbides as a function of the growth temperatures. The latter two structures are easily identified from their chemical composition by EDS analysis of the nanoparticles. This attribution is then confirmed by FFT analyses of HAADF-STEM images of the nanoparticles as in the example given in **Figure 13** for the Co_4W_2C phase. The identification of a Co_2W_4C nanoparticle is shown in the figure S12 in SI.

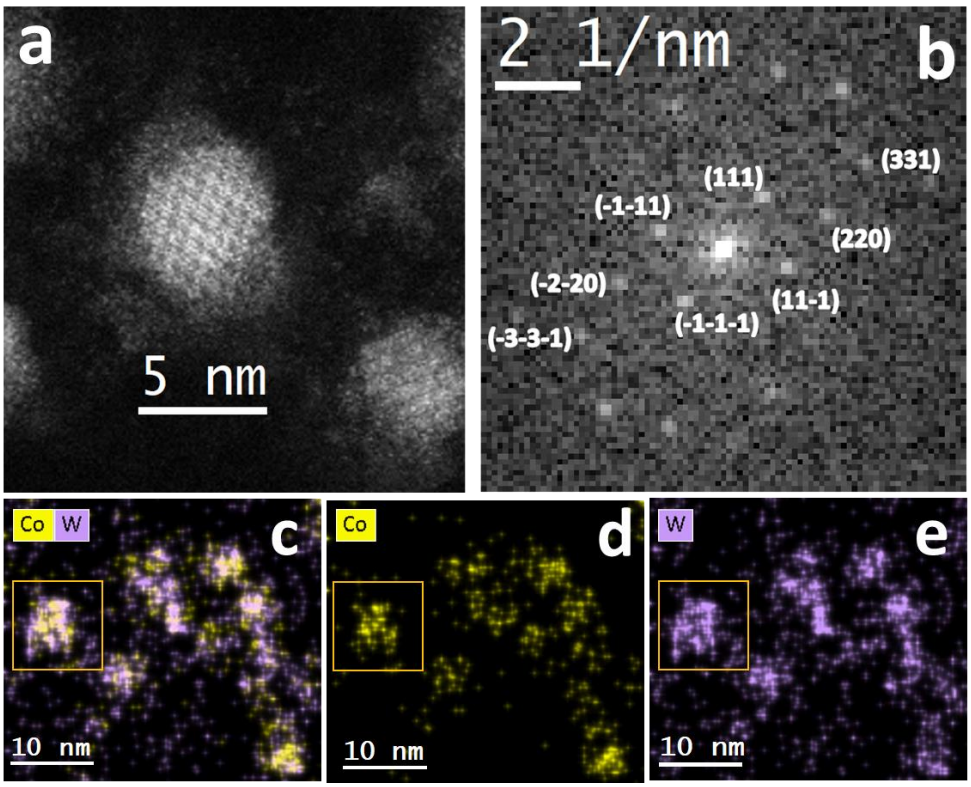

Figure 13. Analysis of a NP with the Co_4W_2C crystal structure (a) HAADF-STEM image of the nanoparticle after heat treatment at 800°C (b) FFT of the image and assignment to the (1-10) zone axis of the Co_4W_2C crystal structure. (c, d and e) EDS elemental mappings of Co in yellow and W in purple. The particle in (a) is highlighted by a square in c, d, and e. Atomic Co:W composition is measured to be 63±5 at.% : 37±5at.%.

The Co_3W_3C and Co_6W_6C compounds are (as for the Co-Mo carbides) difficult to differentiate on the basis of HAADF images when the orientation of the nanoparticle is not favorable. An example of identification of a Co_3W_3C NP is presented in **Figure 14**. HAADF-STEM image simulation was carried out in the same way as for the previous simulation, on the Dr.Probe

software from the crystal structure of Co_3W_3C with the zone axis [011]. The atoms showing the highest intensity are the W atoms. The location of the atoms on the experimental image and the simulation coincide enough to confirm our structure identification for this nanoparticle.

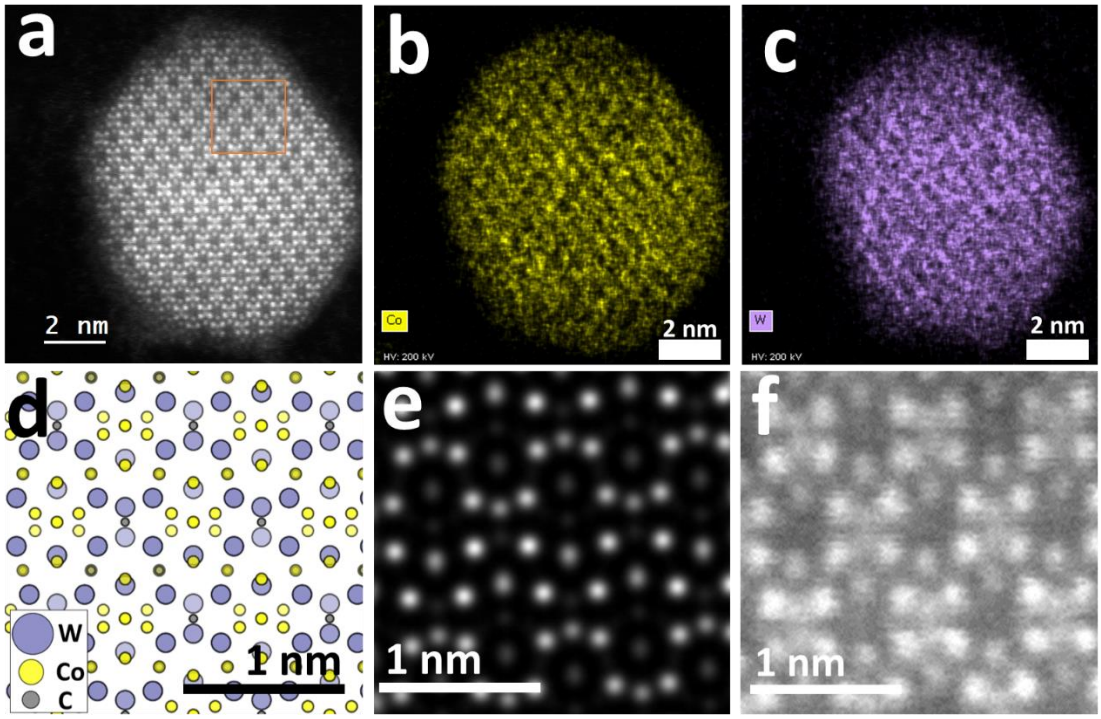

Figure 14. Analysis of a NP with the Co_3Wo_3C structure (a) HAADF-STEM image of the nanoparticle. (b and c) Elemental Co and Mo EDS mappings. (d) Co_3W_3C structure projected along the [110] zone axis. (e) Simulated HAADF-STEM image with Dr.Probe software [41].(f) Magnification of part the experimental image as indicated by the rectangle in (a). The FFT of the HAADF-STEM image and the simulated electron diffraction of the of Co_6Mo_6C in the [110] zone axis is in Figure S13 in SI.

Table 6. Proportion of the different η-carbides from the Cs-Co-W system after pyrolysis as a function of temperature.

Pyrolysis temperature	Co_2W_4C	Co_4W_2C	Co_3W_3C / Co_6W_6C
500°C	11%	22%	67%
600°C	66%	2%	32%
800°C	3%	9%	88%

4. Conclusion

In this paper, a new promising chemical route to the chemical synthesis of bimetallic carbide nanoparticles with chosen composition and low size is proposed. $Co_3M'_3C$, $Co_6M'_6C$, $Co_2M'_4C$ (M'= Mo or W) and Co_4W_2C, metallic carbide nanoparticles were successfully synthesized by thermal decomposition of Cs-Co-M' precursor octacyanometalate networks. The presence of these bimetallic carbides is shown by direct determination of their chemical composition and structure by combining Transmission Electron Microscopy, EDX analysis and high resolution HAADF STEM imaging of individual NPs. The size of these carbide nanoparticles is 5 nm in average. Along with η carbides, the presence of monometallic carbide nanoparticles such as Mo_2C and WC has also been observed. The pyrolysis temperature is an important factor in the formation of nanoparticles. Indeed, a treatment at a too low temperature, below 700°C for Cs-Co-Mo and 800°C for Cs-Co-W will not enable the complete transformation of the precursors. Beyond these temperatures, η-carbide nanoparticles account for the majority of the nanoparticles observed (more than 60%). Their presence in significant proportions in a definite temperature range attests for the efficiency of the synthesis route by thermal decomposition of OCM. The strength of this method also lies in the wide choice of metals that can be used to fabricate octacyanometalate-based networks and thus potentially the wide choice of carbides nanoparticles that could be made easily and rapidly accessible.

5. Experimental Methods

5.1. Octacyanometalate-based network synthesis

Two solutions are prepared. The first one is a 20 mL aqueous solution containing 4 mmol $CoCl_2.6H_2O$ and 8 mmol cesium chloride (CsCl). The second one is a 20 mL aqueous solution containing 4 mmol of $K_4[M'(CN_8)]$ with M'= Mo or W. These two solutions are mixed at ambient temperature under vigorous stirring for 30 min. The resulting solution contains the octacyanometalate network nanoparticles. The products should be kept away from light. The solution is yellow for the Cs-Co-Mo system and orange/red for the Cs-Co-W system. The synthesis of $K_4(M)CN_8$ (M=Mo and W) was performed by ourselves according to the protocol Barth *et al* [42]. Briefly, acetic acid is added dropwise to a water solution of the potassium salt of the chosen molybdate or tungstate, KBH_4 and KCN kept at 40°C. This addition is performed under a continuous argon flow. (This reaction produces highly toxic HCN gas, eliminated by bubbling the argon gas outlet in a two-stage trap combining: 1) a NaOCl-filled bubbler and 2)

a second flask containing solid copper carbonate). Once the addition of acetic acid is over (90 mins), the product is precipitated with ethanol and filtered. The octacyanometalates are obtained as yellow powders.

5.2. TEM Grid preparation

The precursor samples were separated into three batches, and each has undergone heat treatment at one of these temperatures: 500°C, 600°C and 800°C. The precursor samples heat treated at 500°C or 600°C were prepared on Protochip TEM grids to undergo the heat treatment in an ETEM environmental microscope. Those treated at 800°C in a furnace (see below) are prepared on gold TEM grids with a carbon film. On each TEM grid (Protochip and gold grid), a 7nm thick Al_2O_3 alumina layer is deposited before coming to deposit the OCM. After exposing the grids to an argon plasma at 800 W for 4 minutes, the grids are immersed in a millimolar silane solution (**Figure 15**) for 12h. [40]

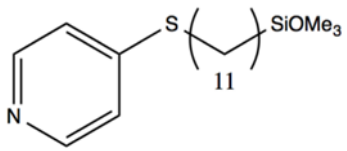

Figure 15. Silane molecule used to attach octacyanometalates-based network nanoparticles to the surface of substrates.

The role of this silane molecule is to attach the OCM precursors of the nanoparticles on the surface of the grid to optimize their distribution. After the immersion in silane, the grids are then washed with anhydrous toluene and dichloromethane to remove the excess silane present on the grids, and are then placed 2h at 100°C. A drop of the OCMs solution is deposited on the TEM grid. The grids are then placed in an oven and heated to the target temperature for heat treatment.

5.3. Materials

For the characterization of the samples, we mainly used Transmission Electron Microscopy (TEM) analysis. Several microscopes were used: FEI-CM 20 TEM (200 kV) to measure the size distribution of the Cs-Co-Mo and Cs-Co-W precursors with a population of 500 nanoparticles in 5 different areas of the grid and counted with the image J software. The UHRSTEM imaging and chemical mappings by EDS were performed using a FEI Titan G2

corrected Cs TEM operated at 200 kV. The energy levels used to identify the elements in EDS analysis are: Co Kα1=6.930 keV ; Mo Lα1= 2.293 keV; W Lα1= 8.397 keV ; Cs Lα1= 4.286 keV ; K Kα1= 3.311 keV ; Cl Kα1= 2.611 keV.

DLS measurements were performed on a Malvern Zetasizer

The calibration of the EDS maps was done with as reference a nanoparticle whose crystal structure corresponded to Co_3W_3C or Co_6Mo_6C and whose ratios between the metals were 1:1. These were used as a reference to determine the percentages of the metals according to the intensity of the EDS signals. The uncertainty of the EDS maps corresponds to the standard deviation of the elemental concentration measured from about 30 nanoparticles of the same structure and chemical composition.

HAADF-STEM image simulations were performed with Dr.Probe code using the following parameters: Uacc = 300.00 kV, alpha = 30.0 mrad, lambda = 1.969 pm, k-alpha = 15.2 1/nm, r-source = 0.040 nm, Delta = 3.0 nm. Detectors: HAADF angular range 200 to 250 mrad. Sample thickness: 5 nm.
The cif files of the crystal structures come from the website *The Materials Project*. [43]

Heat treatments at 500°C and 600°C are performed in a modified Environmental Transmission Electron Microscope (ETEM) FEI-Titan (80-200 keV), equipped with a Cs image aberration corrector. The treatment are done under a nitrogen flow (5 sccm) in order to maintain a neutral atmosphere at a pressure of 5.10^{-3} mbar. Heat treatments at 800°C are performed in a quartz tube placed in a furnace under a nitrogen flow (100 sccm) in order to maintain a neutral atmosphere at a pressure of 90 mbar.

PXRD analysis: data were recorded in the 8-80° 2θ range, at room temperature with an Empyrean PANalytical diffractometer using θ/θ Bragg Brentano geometry. They were measured with a step length of 0.033°(2 θ) using Cu K_α radiation.

TGA measurements were performed on a Setaram SETSYS Evolution model with an TGA/DSC rod. The temperature profile is a 5°C/min ramp to the desired temperature under an argon flux at 20ml/min.

Supporting Information

Supporting Information is available from the Wiley Online Library or from the author.

Acknowledgements

The authors thank ANR GiANT (No. ANR-18-CE09-0014-04).

The HRSTEM-EDS study was carried out within the MATMECA consortium, supported by the ANR-10-EQPX-37 contract and benefited from the facilities of the MSSMat (now LMPS) Laboratory (UMR CNRS 8579), CentraleSup'elec.

The authors acknowledge financial support from the French state managed by the National Research Agency under the Investments for the Future program under the references ANR-10-EQPX-50 pole NanoMax.

The author also thanks the Laboratoire de Physique des Interfaces et Couches Minces (LPICM) of the Ecole Polytechnique, M. Gonclaves, I. Florea and C. Costel-Sorin for their help in the pyrolysis of the samples.

Thanks to Marie-Hélène Vidal (ONERA) for the TGA analysis of the samples.

Thanks to Claire Sanchez (ONERA) for the PXRD analysis of the samples.

Received: ((will be filled in by the editorial staff))

Revised: ((will be filled in by the editorial staff))

Published online: ((will be filled in by the editorial staff))

References

[1] N. Cao, J. Su, W. Luo, G. Cheng, Int J Hydrogen Energy 2014, 39, 9726.

[2] C. D. Mboyi, D. Poinsot, J. Roger, K. Fajerwerg, M. L. Kahn, J. C. Hierso, Small 2021, 17, 1.

[3] M. T. El-Saadony, A. S. ALmoshadak, M. E. Shafi, N. M. Albaqami, A. M. Saad, A. M. El-Tahan, E. S. M. Desoky, A. S. M. Elnahal, A. Almakas, T. A. Abd El-Mageed, A. E. Taha, A. S. Elrys, A. M. Helmy, Saudi J Biol Sci 2021, 28, 7349.

[4] J. Luo, Y. Zhang, S. Zhu, Y. Tong, L. Ji, W. Zhang, Q. Zhang, Q. Bi, Naunyn Schmiedebergs Arch Pharmacol 2021, 394, 1991.

[5] K. Zhou, X. Zhou, J. Liu, Z. Huang, J Pet Sci Eng 2020, 188, 106943.

[6] E. Hao, G. C. Schatz, J. T. Hupp, J Fluoresc 2004, 14, 331.

[7] R. Narayanan, M. A. El-Sayed, Journal of Physical Chemistry B 2005, 109, 12663.

[8] C. Bracey, P. Ellis, G. Hutchings, Chem Soc Rev 2009, 38, 2231.

[9] G. Niu, M. Zhou, X. Yang, J. Park, N. Lu, J. Wang, M. J. Kim, L. Wang, Y. Xia, Nano Lett 2016, 16, 3850.

[10] T. Mitsudome, K. Kaneda, Green Chemistry 2013, 15, 2636.
[11] A. Schatz, O. Reiser, W. J. Stark, Chemistry - A European Journal 2010, 16, 8950.
[12] B. M. Tackett, W. Sheng, J. G. Chen, Joule 2017, 1, 253.
[13] M. Yamauchi, H. Kobayashi, H. Kitagawa, ChemPhysChem 2009, 10, 2566.
[14] L. H. Bennett, J. R. Cuthill, A. J. Mcalister, N. E. Erickson, R. E. Watson, Science (1979) 1974, 184, 563.
[15] S. T. Hunt, T. Nimmanwudipong, Y. Román-Leshkov, Angewandte Chemie 2014, 126, 5231.
[16] Z. Zhou, Z. Yuan, S. Li, H. Li, J. Chen, Y. Wang, Q. Huang, C. Wang, H. E. Karahan, G. Henkelman, X. Liao, L. Wei, Y. Chen, Small 2019, 15, 1.
[17] H. Vrubel, X. Hu, Angewandte Chemie - International Edition 2012, 51, 12703.
[18] S. Izhar, M. Nagai, J Power Sources 2008, 182, 52.
[19] X. Ma, H. Meng, M. Cai, P. K. Shen, J Am Chem Soc 2012, 134, 1954.
[20] H. Yoshida, S. Takeda, T. Uchiyama, H. Kohno, Y. Homma, Nano Lett 2008, 8, 2082.
[21] H. An, A. Kumamoto, R. Xiang, T. Inoue, K. Otsuka, S. Chiashi, C. Bichara, A. Loiseau, Y. Li, Y. Ikuhara, S. Maruyama, Atomic-Scale Structural Identification and Evolution of Co-W-C Ternary SWCNT Catalytic Nanoparticles: High-Resolution STEM Imaging on SiO 2, 2019.
[22] M. Abou Hamdan, S. Loridant, M. Jahjah, C. Pinel, N. Perret, Appl Catal A Gen 2019, 571, 71.
[23] M. Zheng, J. Pang, R. Sun, A. Wang, T. Zhang, ACS Catal 2017, 7, 1939.
[24] A. M. Nartowski, I. P. Parkin, M. MacKenzie, A. J. Craven, I. MacLeod, J Mater Chem 1999, 9, 1275.
[25] A. M. Nartowski, I. P. Parkin, A. J. Craven, M. MacKenzie, Advanced Materials 1998, 10, 805.
[26] R. F. André, F. D'Accriscio, A. P. Freitas, G. Crochet, C. Bouillet, M. Bahri, O. Ersen, C. Sanchez, S. Carenco, Green Chemistry 2021, 23, 6431.
[27] J. M. Newsam, A. J. Jacobson, L. E. Mccandlish, R. S. Polizzotti, The Structures of the η-Carbides N6MO6C, Co6M06C, and Co6Mo6C2, 1988.
[28] S. Korlann, B. Diaz, M. E. Bussell, Chemistry of Materials 2002, 14, 4049.
[29] S. Alconchel, F. Sapiña, E. Martínez, Dalton Transactions 2004, 2463.
[30] L. Catala, T. Mallah, Coord Chem Rev 2017, 346, 32.
[31] D. Brinzei, L. Catala, G. Rogez, A. Gloter, T. Mallah, Inorganica Chim Acta 2008, 361, 3931.
[32] T. Hozumi, K. Hashimoto, S. I. Ohkoshi, J Am Chem Soc 2005, 127, 3864.
[33] C. Aparicio, L. Machala, Z. Marusak, in J Therm Anal Calorim, 2012,110 , 661.
[34] D. Brinzei, L. Catala, N. Louvain, G. Rogez, O. Stéphan, A. Gloter, T. Mallah, J Mater Chem 2006, 16, 2593.
[35] F. Volatron, D. Heurtaux, L. Catala, C. Mathonière, A. Gloter, O. Stéphan, D. Repetto, M. Clemente-León, E. Coronado, T. Mallah, Chemical Communications 2011, 47, 1985.
[36] Topas V5.0: General Profile and Structure Analysis Software for Powder Diffraction Data, Bruker AXS Ltd, 2014.
[37] K. Imoto, D. Takahashi, Y. Tsunobuchi, W. Kosaka, M. Arai, H. Tokoro, S. I. Ohkoshi, Eur J Inorg Chem 2010, 4079.
[38] J. M. Herrera, A. Bleuzen, Y. Dromzée, M. Julve, F. Lloret, M. Verdaguer, Inorg Chem 2003, 42, 7052.
[39] M. B. Zakaria, T. Chikyow, Coord Chem Rev 2017, 352, 328.
[40] S. Forel, A. Castan, H. Amara, I. Florea, F. Fossard, L. Catala, C. Bichara, T. Mallah, V. Huc, A. Loiseau, C. S. Cojocaru, Nanoscale 2019, 11, 3952.
[41] J. Barthel, Ultramicroscopy 2018, 193, 1.

[42] J. A. Barth, J. G. Leipoldt, L. D. C. Bok, P. J. Cilliers, Z. anorg. allg. Chem, 1974, 407, 350
[43] https://materialsproject.org/
[44] Y. Seto, M. Ohtsuka, J Appl Crystallogr 2022, 55, 397.
[45] K. Kuo, Acta Metallurgica 1953, 1, 301.
[46] C. B. Pollock, H. H. Stadelmaier, Metallurgical Transactions 1970 1:4 1970, 1, 767.
[47] P. Ettmayer, R. Suchentrunk, Monatshefte für Chemie / Chemical Monthly 1970 101:4 1970, 101, 1098.
[48] V. Adelsköld, A. Sundelin, A. Westgren, Z Anorg Allg Chem 1933, 212, 401.

Supporting Information

η-carbides (Co, Mo or W) nanoparticles from octacyanometalates precursors-based network

Thomas Blin [1,2], Armelle Girard [1,3], Frédéric Fossard[1], Nathalie Guillou[3], Laure Catala[2], Annick Loiseau[1], Vincent Huc[2]*

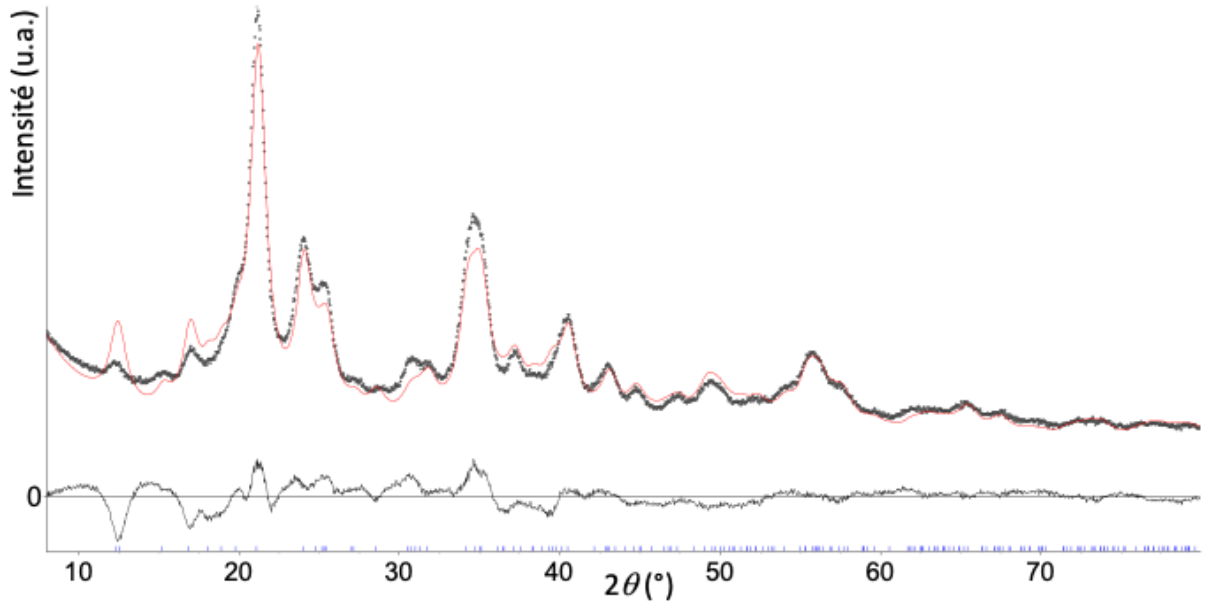

Figure S1. Final Rietveld plot of $Cs_2Co_7[Mo(CN)_8]_4 \cdot 6H_2O$ showing observed (black dotes), calculated (red line), and difference (black line) curves (λ = 1.5418 Å).

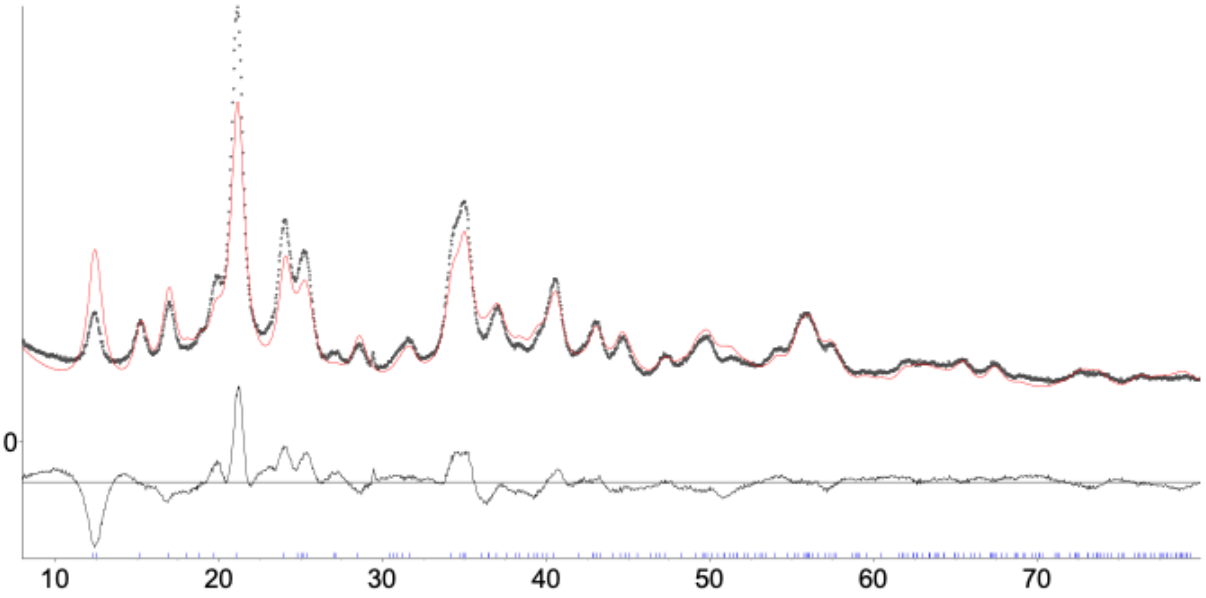

Figure S2. Final Rietveld plot of $Cs_2Co_7[W(CN)_8]_4 \cdot 6H_2O$ showing observed (black dotes), calculated (red line), and difference (black line) curves (λ = 1.5418 Å).

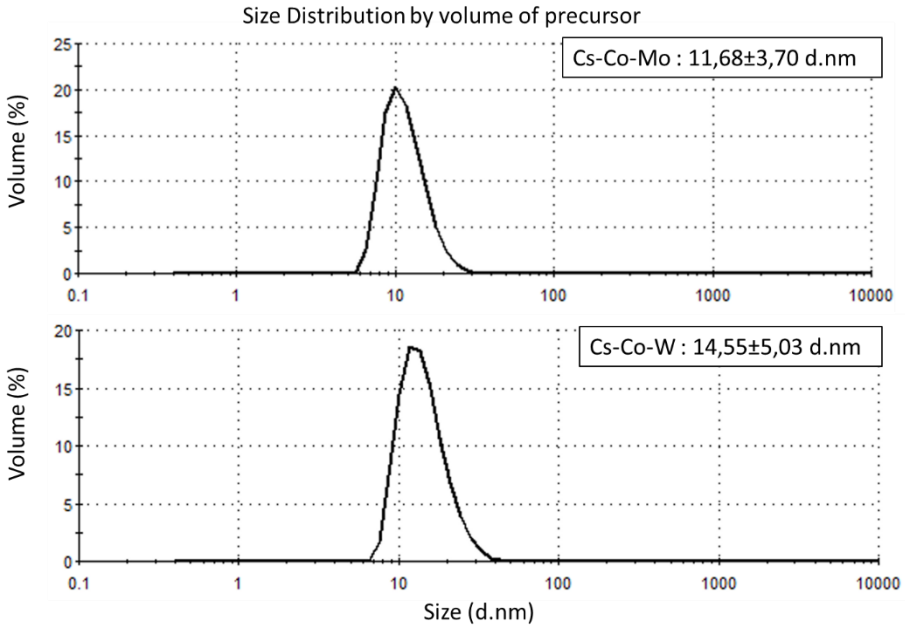

Figure S3. Hydrodynamic size distribution by volume of the OCMS nanoparticles in water obtained by DLS on an as-synthesized dispersion

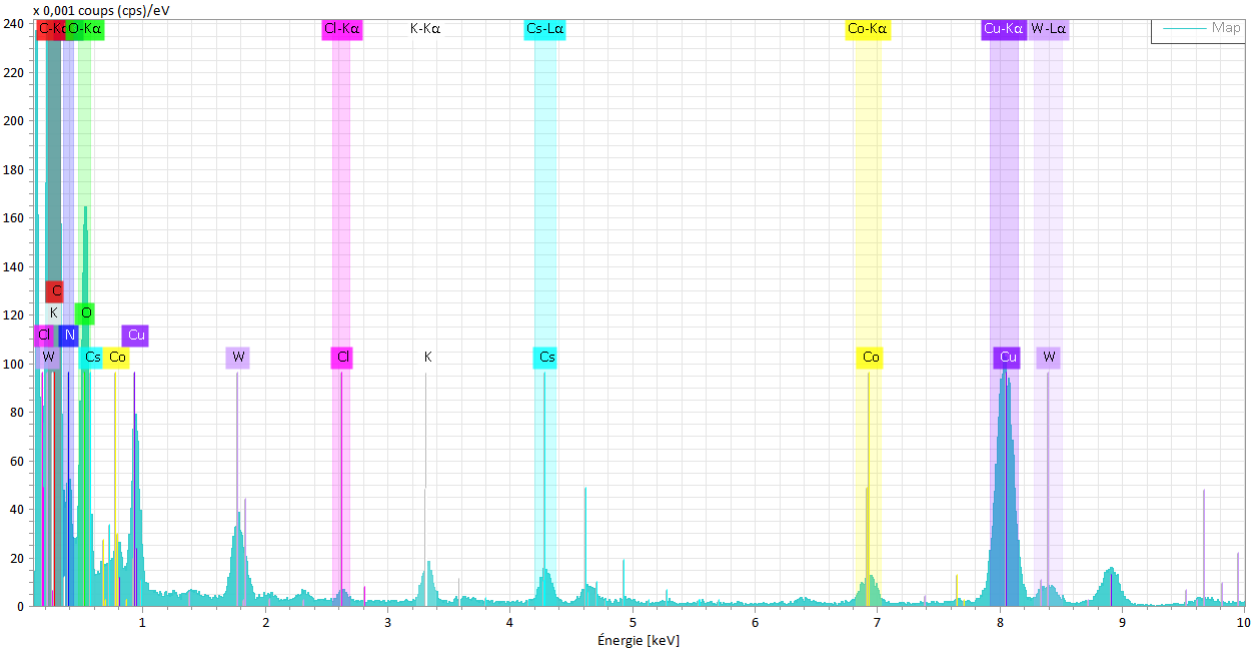

Figure S4. EDS spectrum of the mapping of figure 4. Cs is present in the chemical composition before pyrolysis. The presence of Cu is explained by the composition of the microscope's object holder and the TEM grid.

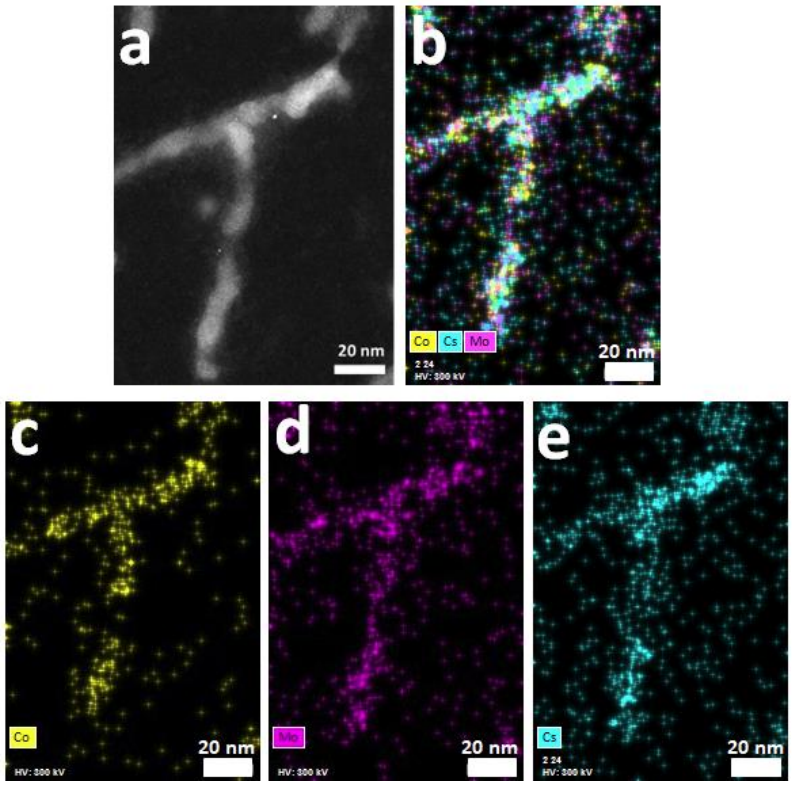

Figure S5. (a) Cs-Co-Mo OCM network HAADF-STEM image. (b), (c), (d) and (e) Corresponding EDS elemental mappings of Co-Mo-Cs, Co, Mo and Cs respectively (Co Kα1=6.930 KeV, Mo Lα1= 2.293 keV, Cs Lα1= 4.286 keV

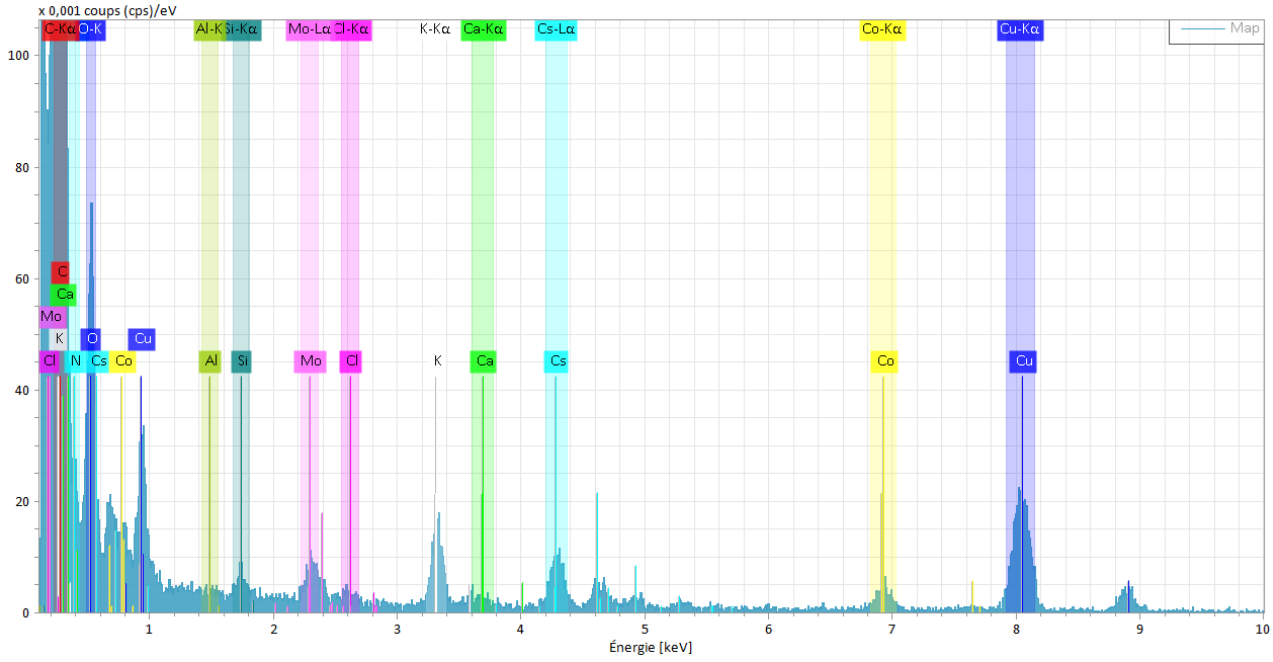

Figure S6. EDS spectrum of the mapping of figure 5. Cs is present in the chemical composition before pyrolysis. The presence of Cu is explained by the composition of the microscope's object holder and the TEM grid.

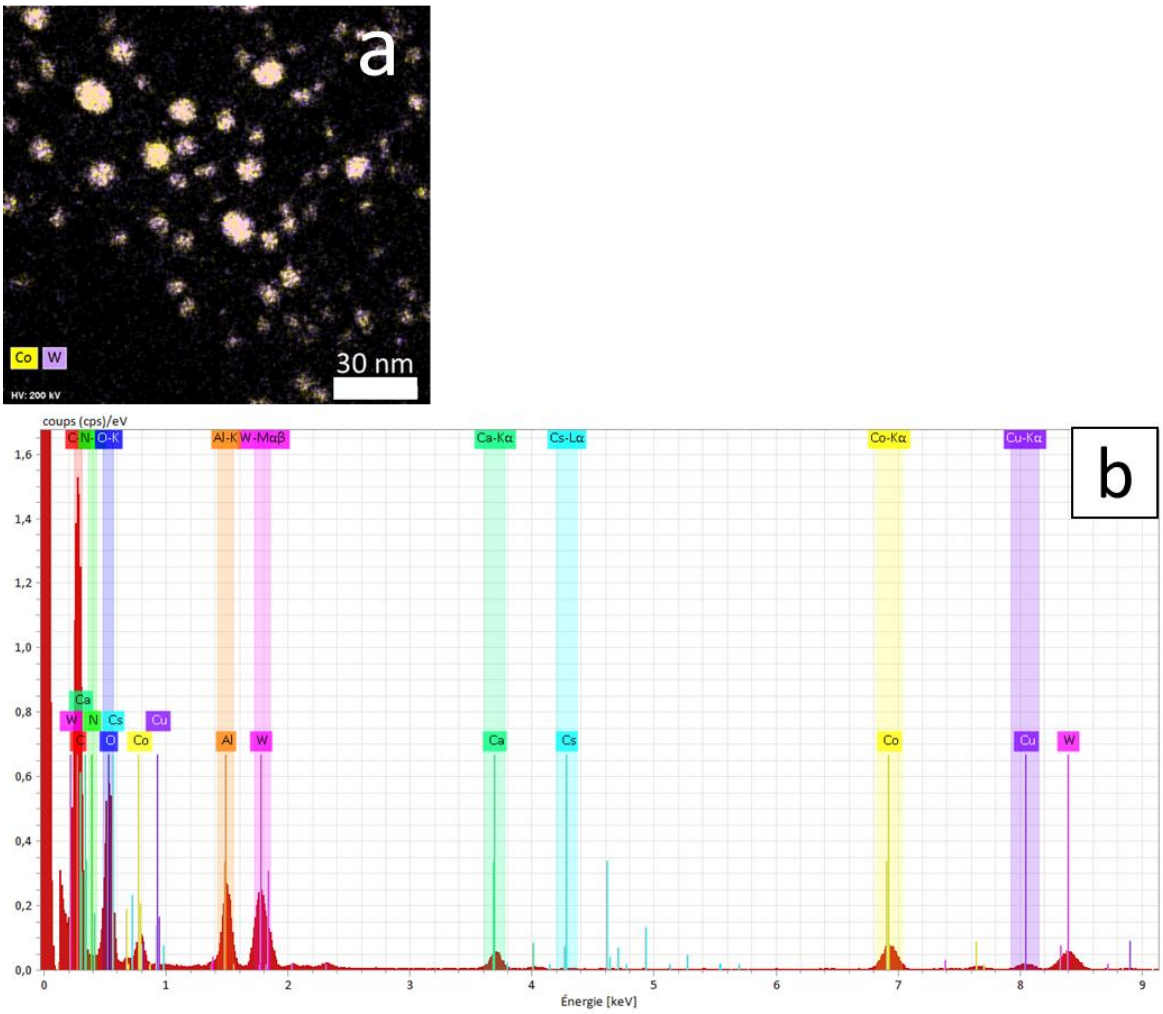

Figure S7. (a) Chemical mappings using EDS mode for Co-W system after pyrolysis under N_2 at 800°C. (b) EDS spectrum. Cs is not present in the chemical composition after pyrolysis. The presence of Al is explained by the alumina layer on the substrate, Cu by the composition of the microscope's object holder and the TEM grid and Ca by the use we have made of it to precipitate the precursors in powder form.

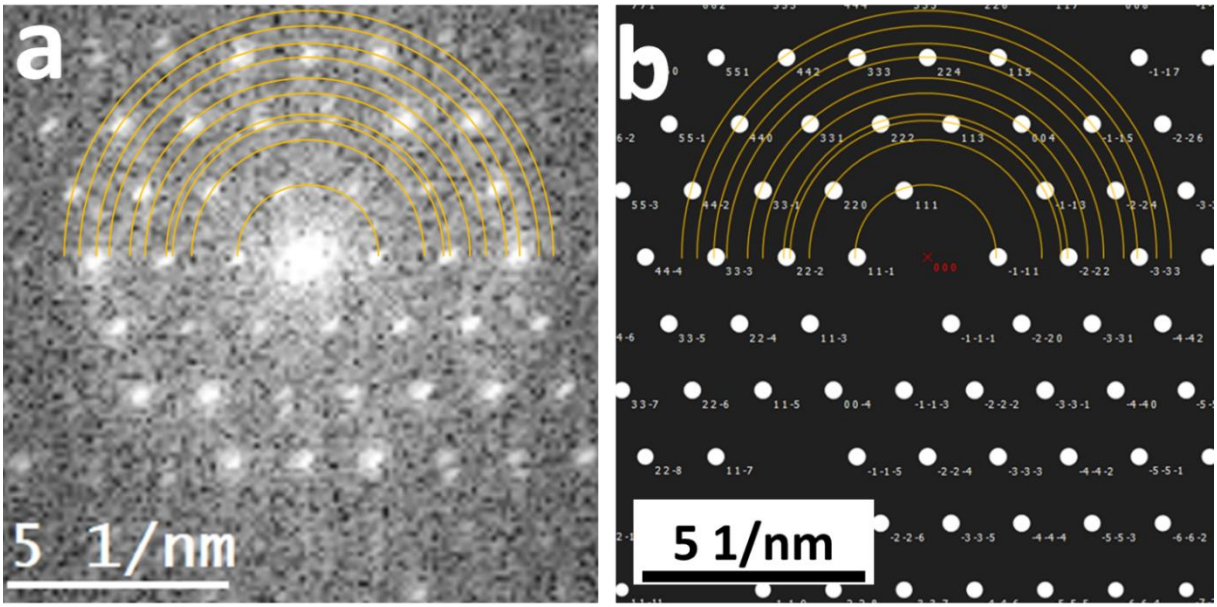

Figure S8. (a) FFT of the Co_6Mo_6C nanoparticle imaged in figure 10. (b) Simulation of Co_6Mo_6C 300 KeV electron diffraction pattern of the structure projected along the [110] axis, using ReciPro software [44].

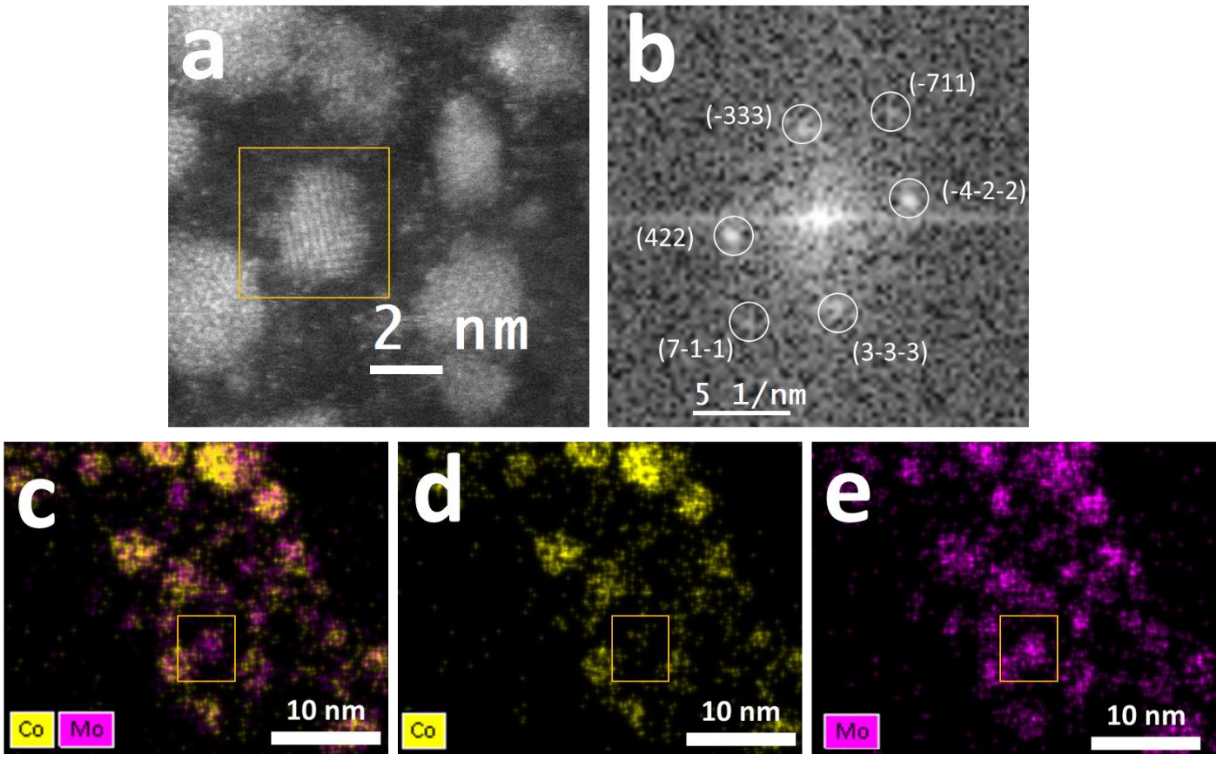

Figure S9. HAADF image of a nanoparticle marked by the yellow square and identified as the Co_2Mo_4C structure projected along the [01-1] axis (b) FFT of the squared NP in (a) with identification of the (422), (333) and (711) plane families of the Co_2Mo_4C crystal structure. (c, d, and e) EDS analysis of the squared NP in (a) showing the spatial distribution of Co (31±5 at. %) in yellow and Mo (69±5 at. %) within the nanoparticle marked.

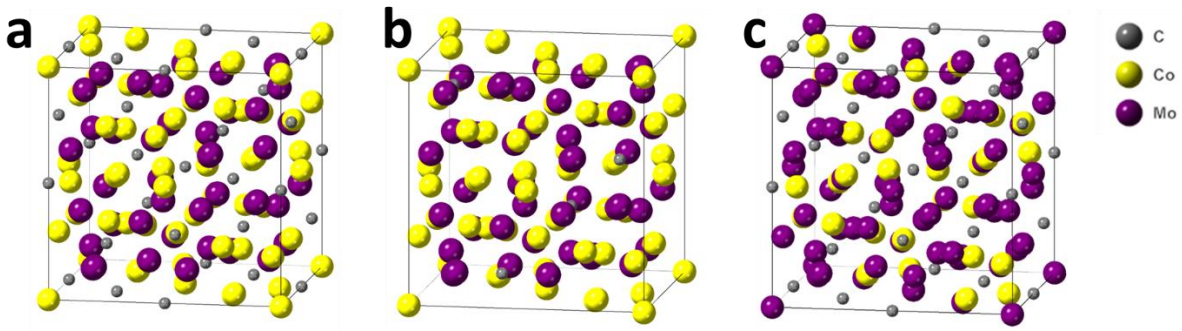

Figure S10. Representations of the crystal structures of compounds (a) Co_3Mo_3C (b) Co_6Mo_6C (c) Co_2Mo_4C. Color labels are C in grey, Co in yellow and Mo in purple**.**

Table S1. Crystallographic data from the literature of bimetallic carbides of the Cs-Co-Mo system

η-carbide	Space group	*a* (Å)	*V* (Å3)	reference
Co_3Mo_3C	$Fd\bar{3}m$	11.08	1357	[25]
Co_6Mo_6C	$Fd\bar{3}m$	10.90	1295	[25]
Co_2Mo_4C	$Fd\bar{3}m$	11.25	1423	[45]

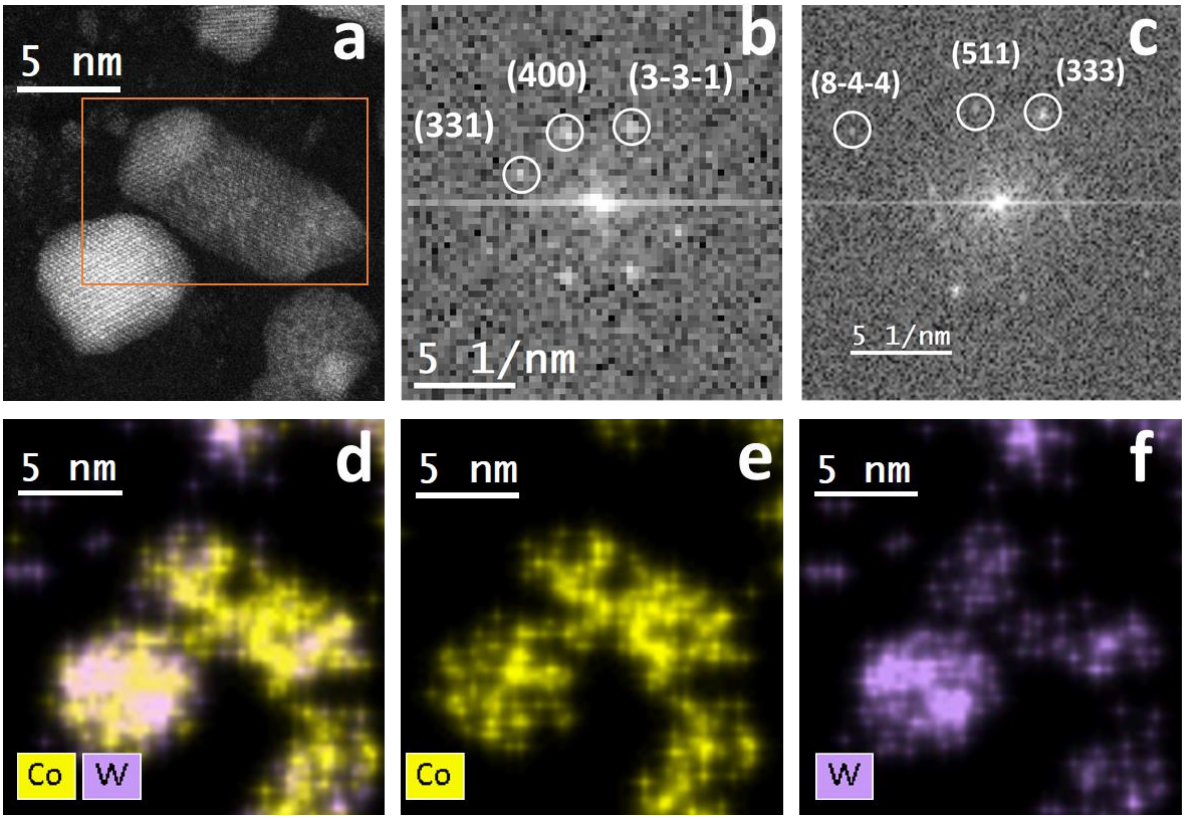

Figure S11. (a) HAADF-UHRSTEM image of a Janus nanoparticle marked by the orange square. The left side is identified as the Co_3W_3C or Co_6W_6C structure and the right side is identified as the Co_4W_2C structure (b) FFT of the left-hand side of the nanoparticle projected along the [0-13] axis. (b) FFT of the right-hand side of the nanoparticle projected along the [01-1] axis. (d, e and f)) EDS analysis of the the Janus NP showing the spatial distribution of Co in yellow and W. the left side showing as composition Co 55±5 at.% and W 45±5 at.%. The right side showing as composition Co 71±5 at. % and W 29±5 at.%.

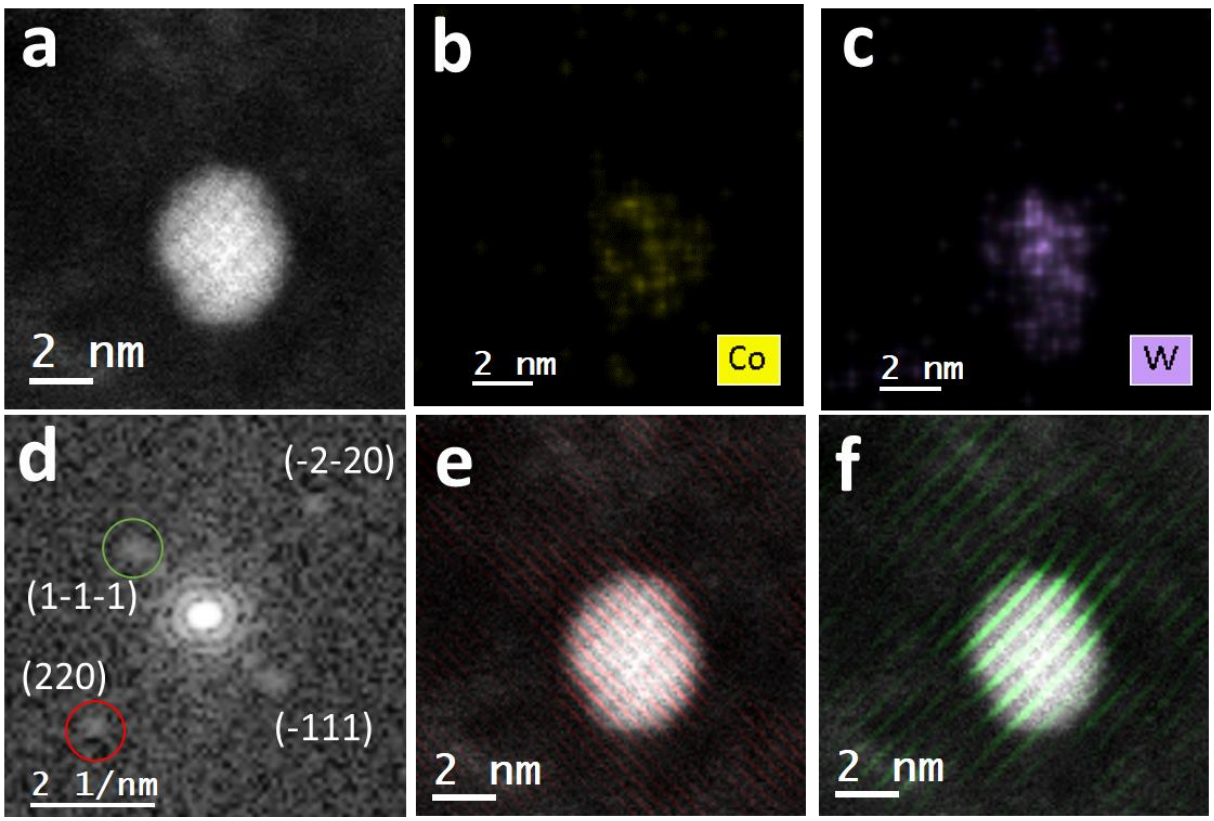

Figure S12. (a) HAADF image of the nanoparticle identified with the Co_2W_4C structure. (b and c) EDS elemental maps of Co in yellow (37±5 at. %) and W in purple (63±5 at.%) within the nanoparticle (d) FFT with identification of the (111) and (220) plane families of the Co_2W_4C crystal structure. Highlighted plan by FFT (e) (220) and (f) (1-1-1).

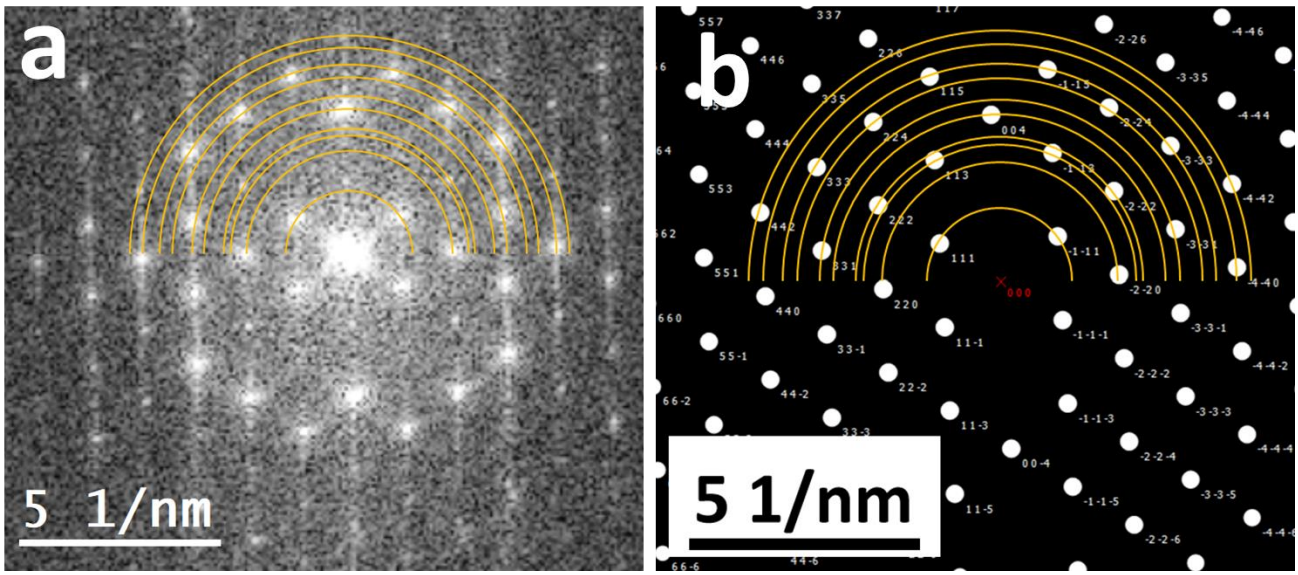

Figure S13. FFT of the HAADF nanoparticle image in figure 15. (b) simulation of a Co_3W_3C 300KeV electron diffraction pattern of the structure projected along [110] axis, using ReciPro software [44]

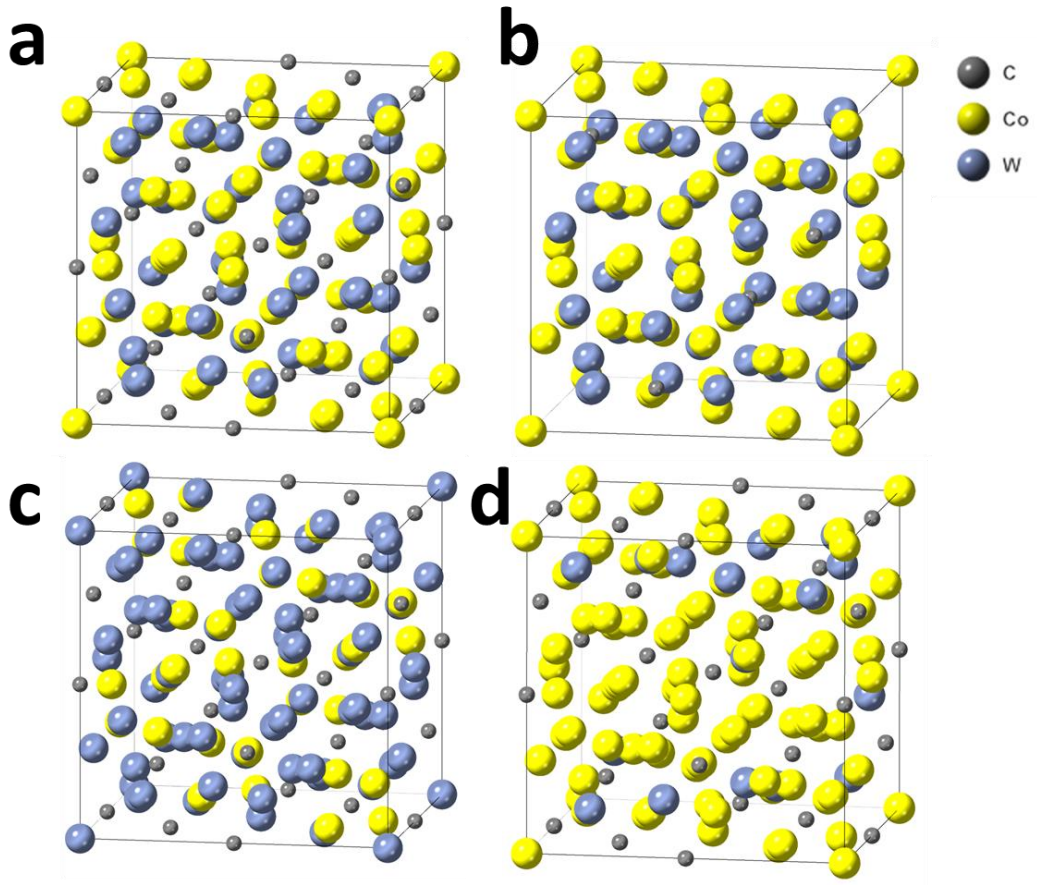

Figure S14. Representations of the crystal structures of compounds (a) Co_3W_3C (b) Co_6W_6C (c) Co_2W_4C (d) Co_4W_2C. Color labels are grey for C, yellow for Co and blue for W.

Table S2. Crystallographic data from the literature of bimetallic carbides of the Cs-Co-W system

η-carbide	Space group	a (Å)	V (Å3)	reference
Co_3W_3C	$Fd\bar{3}m$	11.11	1370	[46]
Co_6W_6C	$Fd\bar{3}m$	10.90	1296	[47]
Co_2W_4C	$Fd\bar{3}m$	11.24	1420	[47]
Co_4W_2C	$Fd\bar{3}m$	11.01	1335	[48]